*This manuscript has been accepted for publication in the journal Chemical Geology*
*https://doi.org/10.1016/j.chemgeo.2021.120610*

# Improving the reliability of Fe- and S-XANES measurements in silicate glasses: Correcting beam damage and identifying Fe-oxide nanolites in hydrous and anhydrous melt inclusions

Allan H. Lerner[1*], Michelle J. Muth[1], Paul J. Wallace[1], Antonio Lanzirotti[2], Matthew Newville[2], Glenn A. Gaetani[3], Proteek Chowdhury[4], Rajdeep Dasgupta[5]

[1] Department of Earth Sciences, University of Oregon, Oregon 97403, USA

[2] Center for Advanced Radiation Sources, The University of Chicago, Illinois 60637, USA

[3] Department of Geology and Geophysics, Woods Hole Oceanographic Institution, Woods Hole, Massachusetts 02543, USA

[4] Department of Earth and Planetary Sciences, University of California, Riverside, CA 92521, USA

[5] Department of Earth, Environmental, and Planetary Sciences, Rice University, Texas 77005, USA

[*] Corresponding author at: 1272 University of Oregon, Eugene, OR 97403, USA. *E-mail address:* lerner.allan@gmail.com (A. H. Lerner).

## Highlights

- Photo-oxidation during Fe-XANES analyses of glasses can be corrected by time-dependent restorations to initial values
- Photo-reduction can occur rapidly during S-XANES analyses even in glasses that are stable during Fe-XANES analysis
- Photo-reduction during S-XANES can be corrected by restoring $S^{4+}$ to $S^{6+}$ signal intensities
- Fe-oxide nanolites in otherwise glassy melt inclusions can be identified by magnetite-like features in Fe-XANES spectra
- Beam damage correction techniques enable accurate XANES measurements of damage-susceptible glasses and melt inclusions

**Abstract**

The redox state of silicate melts influences crystallization, element partitioning, and degassing behavior. Synchrotron-based micro-X-ray absorption near edge structure (μXANES) spectroscopy has emerged as a powerful tool for determining redox conditions through the direct measurement of speciation of multivalent elements such as iron and sulfur in silicate glasses. In particular, the high spatial resolution afforded by synchrotron μXANES makes it one of the few techniques available for determining redox conditions in melt inclusions, which can provide insights into pre-eruptive melt properties. However, the small size of melt inclusions, the deep penetration of X-rays, and irradiation-induced beam damage make μXANES measurements in melt inclusions challenging. Here we present data that show rapid Fe- and S-μXANES beam damage in experimental glasses, mid-ocean ridge basalt glasses, and olivine-hosted melt inclusions from the southern Cascade arc and Kīlauea Volcano and develop approaches to recognize and correct for beam damage through repeated rapid analyses. By applying a time-dependent correction to a series of rapid measurements (~82 s/scan) of Fe-μXANES pre-edge centroid positions, irradiation-induced photo-oxidation ($Fe^{2+}$ to $Fe^{3+}$) can be corrected back to undamaged initial $Fe^{3+}/\Sigma Fe$ even in damage-susceptible hydrous glasses. Using this beam damage correction technique, hydrous basaltic melt inclusions from the southern Cascades have $Fe^{3+}/\Sigma Fe$ that is ~0.036 lower (corresponding to -0.5 log units lower oxygen fugacity) than would have been indicated by standard Fe-μXANES measurements. Repeated, rapid analyses (150 – 300 s/scan) were used to identify S-μXANES beam damage (photo-reduction of $S^{6+}$ to $S^{4+}$), which was corrected with a peak fitting method to restore initial $S^{6+}/\Sigma S$. We observe that S-μXANES beam damage can occur rapidly even in low-$H_2O$ mid-ocean ridge basaltic glasses and melt inclusions from Kīlauea Volcano, which are otherwise stable during even prolonged Fe-μXANES analyses. By mitigating and correcting for sulfur photo-reduction, we conclude that some mid-ocean ridge basaltic glasses contain 0.08 – 0.09 $S^{6+}/\Sigma S$, which is more sulfate than might be expected based on the reduced oxidation state of these glasses (near the fayalite-magnetite-quartz oxygen buffer). Using beam damage identification and correction techniques, the valence states of iron and sulfur can be accurately measured even in beam damage-susceptible glasses and melt inclusions. Finally, using Fe-μXANES, we demonstrate the presence of Fe-oxide nanolites within otherwise glassy, naturally quenched melt inclusions, which can complicate determination of iron valence state in affected glasses.

**Key words:** XANES; Beam Damage; Nanolites; Sulfur; Iron; Melt Inclusions

## 1 Introduction

Synchrotron-based micro-X-ray absorption near edge structure (μXANES) spectroscopy has become a valuable petrologic tool for *in situ* determination of the valence state and molecular complexing of redox-sensitive elements in magmatic minerals and glasses (see review by Sutton et al., 2020). In particular, Fe- and S-μXANES have been applied to quenched volcanic glasses to advance our understanding of magmatic oxygen fugacity ($fO_2$) and complexing of species in glasses from Earth's mid-ocean ridges, hotspots, and volcanic arcs (Bonnin-Mosbah et al., 2001, 2002; Wilke et al., 2006; Berry et al., 2008; Kelley and Cottrell, 2009; Cottrell and Kelley, 2011; Brounce et al., 2014, 2017; Dyar et al., 2016; Lanzirotti et al., 2019; Moussallam et al., 2019; Sutton et al., 2020), as well as in igneous material from lunar and Martian samples (Righter et al., 2013; McCanta et al., 2017, 2019). The $fO_2$ of magmas exerts a major control on mineral stability and thereby the differentiation paths of magmas (Osborn, 1959; Kelley and Cottrell, 2012), including the behavior of important ore-forming species (e.g. Cr, Cu, Fe, Ti; Papike et al., 2016; Lanzirotti et al., 2019; Sutton et al., 2020). Additionally, $fO_2$ can significantly affect the solubility and degassing of multivalent volatiles (e.g., S, C) (Jugo, 2009; Jugo et al., 2010; de Moor et al., 2013; Jégo and Dasgupta, 2014; Moussallam et al., 2014, 2016; Helz et al., 2017; Head et al., 2018). A well-established approach to determining melt $fO_2$ is by measuring $Fe^{3+}/\Sigma Fe$ in quenched glasses (e.g., Kress and Carmichael, 1991; Borisov et al., 2018; O'Neill et al., 2018).

Iron occurs as both $Fe^{2+}$ and $Fe^{3+}$ in most terrestrial melts, and as $Fe^{2+}$ or $Fe^{0}$ in strongly reduced melts below the IW buffer (generally extraterrestrial) (Schreiber et al., 1987). Fe-XANES allows the mean valence state of iron in minerals and silicate glasses to be determined based on spectral features at energies below the iron absorption edge (pre-edge features), while higher energy features inform iron bonding coordination in minerals (e.g., Waychunas et al., 1983; Bajt et al., 1994; Wilke et al., 2001, 2004, 2006; Berry et al., 2003, 2008; Farges et al., 2004; Cottrell et al., 2009). Fe-XANES pre-edge features in glasses are specifically sensitive to valence state, and measured spectra can therefore be related to glass $Fe^{3+}/\Sigma Fe$ by comparison to

suites of glass standards synthesized under controlled redox conditions and analyzed using Mössbauer spectroscopy (e.g., Berry et al., 2003; Wilke et al., 2004; Cottrell et al., 2009). Several published calibrations relate measured Fe-XANES spectral centroid position associated with $Fe^{2+}$ and $Fe^{3+}$ pre-edge peaks to $Fe^{3+}/\Sigma Fe$ in silicate glasses (Galoisy et al., 2001; Bonnin-Mosbah et al., 2001; Berry et al., 2003; Wilke et al., 2004, 2007; Cottrell et al., 2009; Dauphas et al., 2014; Zhang et al., 2016, 2018; Fiege et al., 2017). Other recent calibrations have used multivariate analysis of the entire Fe-XANES spectrum to determine iron valence in standard glasses measured by Mössbauer (Shorttle et al., 2015; Dyar et al., 2016).

Sulfur in silicate melts dominantly occurs as $S^{2-}$ or $S^{6+}$ (Carroll and Rutherford, 1988; Wilke et al., 2008). The transition between $S^{2-}$ and $S^{6+}$ species in silicate melts occurs over a relatively narrow $fO_2$ range near the Ni-NiO buffer (Carroll and Rutherford, 1988; Jugo et al., 2010; Botcharnikov et al., 2011), although there is evidence that this transition is dependent on pressure, temperature, and melt composition (Baker and Moretti, 2011; Klimm et al., 2012a; Fiege et al., 2014; Masotta and Keppler, 2015; Matjuschkin et al., 2016; Nash et al., 2019). S-XANES has been used to quantify the $S^{6+}/\Sigma S$ in glasses by fitting the relative intensity of absorption peaks for sulfide and sulfate species that occur at ~2475 – 2479 and ~2481 – 2483 eV, respectively (Paris et al., 2001; Métrich et al., 2002, 2009; Bonnin-Mosbah et al., 2002; Fleet et al., 2005; Jugo et al., 2010). These two sulfur species generally have distinct spectral absorbance features when present in silicate glasses. Based on melt composition and cooling history, reduced sulfur can also occur in a variety of metal-sulfide complexes, each of which has particular identifiable spectroscopic features (Li et al., 1995; Bonnin-Mosbah et al., 2002; Fleet et al., 2005; Head et al., 2018).

Fe- and S-XANES are particularly powerful techniques for investigating redox conditions of melt inclusions (MI), which are small parcels of quenched glass formed from melt entrapped within growing crystals. Melt inclusions are useful because they can preserve information on volatile concentrations and melt diversity that is otherwise lost during magma mixing, ascent, and eruption (Kent, 2008; Métrich and Wallace, 2008; Wallace et al., 2021). Melt inclusions in many systems of petrologic interest have mean diameters of 10 – 100 μm. The small size of MI leaves μXANES (hereafter XANES) as one of the few techniques suitable for *in situ* measurements of element speciation (i.e., valence state and molecular coordination) within MI.

Of course, inferring magma redox state from iron and sulfur valence in quenched glasses requires accurate XANES measurements. The large penetrative depths of high-energy X-rays and oblique incident beam trajectories at many analytical facilities require careful sample preparation and analytical strategies to avoid signal contamination during Fe- and S-XANES measurements of MI and matrix glasses (Figure 1). It has also been recognized that many glass compositions are susceptible to X-ray induced changes in iron and sulfur speciation during analysis (i.e., beam damage) (Wilke et al., 2008; Métrich et al., 2009; Gonçalves Ferreira et al., 2013; Moussallam et al., 2014, 2019; Cottrell et al., 2018; Blundy et al., 2020; Hughes et al., 2020). Although Fe-XANES measurements of nominally anhydrous basaltic and rhyolitic glasses are observed to be reproducible over a broad range of incident X-ray fluxes (Cottrell et al., 2009), hydrous volcanic glasses, particularly basaltic compositions, have been observed to undergo rapid oxidation of $Fe^{2+}$ to $Fe^{3+}$ with progressive irradiation (Cottrell et al., 2018; Moussallam et al., 2019). The exact mechanisms of iron photo-oxidation are not fully understood, but involve the production of photoelectrons and the local accumulation of charge in non-conductive materials, which alters the electron state of multivalent elements. The ensuing redox exchanges within glasses are accelerated by O-H volatilization or migration (Cottrell et al., 2018).

S-XANES measurements in silicate glasses have also been observed to undergo beam-induced changes in speciation, typically with $S^{6+}$ being reduced to $S^{4+}$ during progressive X-ray irradiation (Wilke et al., 2008; Métrich et al., 2009). Strategies to mitigate beam damage during Fe- and S-XANES measurements include reducing X-ray flux density (photon flux/analytical area) by using defocused beams, continually moving the sample during analysis, and/or decreasing incident photon flux (Wilke et al., 2008; Métrich et al., 2009; Klimm et al., 2012a; Brounce et al., 2017; Cottrell et al., 2018; Moussallam et al., 2019). Spatially resolved XANES beamlines are available at a number of synchrotron light sources worldwide with incident X-ray intensities ranging from $10^8 – 10^{12}$ photons/s (Sutton et al., 2020), where higher X-ray fluxes shorten analysis time by providing lower detection limits, but amplify beam damage concerns.

Many of these approaches to lessen beam damage are challenging to apply to MI owing to their small sizes. Smaller MI require more focused beam diameters to avoid contamination by the host-phase, but are thereby subject to higher photon densities and thus possible beam damage (e.g., Gaborieau et al., 2020; Tassara et al., 2020). Melt inclusions are often targeted for

petrological investigation specifically because they can retain magmatic volatiles that are otherwise lost from the external magma during ascent and degassing (Kent, 2008; Métrich and Wallace, 2008). However, silicate glasses with high $H_2O$ content have been observed to undergo larger changes in iron (and potentially sulfur) speciation during irradiation than what is observed in anhydrous silicate glasses (Cottrell et al., 2018; Moussallam et al., 2019). Hydrous MI may also be susceptible to the formation of nanolite crystals during quenching (Danyushevsky et al., 2002; Di Genova et al., 2018), which may lead to spurious interpretation of XANES spectra. These combined properties make it particularly challenging to apply XANES oxybarometry methods to the analysis of MI from volcanic arc environments, which tend to be both small and $H_2O$-rich.

For these more challenging MI, it is beneficial to develop XANES approaches that both minimize changes in elemental speciation during irradiation and correct for changes that do occur. Applying generalized corrections to datasets is not ideal because differences in glass compositions and $H_2O$ contents (e.g., caused by variable diffusive $H^+$ loss from MI before quenching) can lead to different MI susceptibilities to beam damage within the same deposit or even within the same host mineral.

In this study, we present techniques that aid in recognizing X-ray--induced changes in iron and sulfur valence in volcanic glasses and MI that result from XANES analysis. We then propose new time-dependent corrections for beam damage that does occur. For S-XANES, we also introduce a new spectral fitting approach that may better account for reduction of $S^{6+}$ to $S^{4+}$ during analysis. Finally, we present a method to identify the presence of Fe-oxide nanolites in MI during Fe-XANES analysis. Collectively, these methods enable reliable quantification of iron and sulfur valence, and thereby melt redox state, from small and/or beam damage-susceptible glasses and MI.

## 2.1 XANES analysis of melt inclusions

### 2.1.1 Geometric considerations

At the Fe *K*-edge, the characteristic 1/e X-ray absorption depth in basaltic glass is ≈ 40 μm (Elam et al., 2002), and 120 μm ($1/e^3$) thick glass is therefore required for 95% absorption of X-rays during Fe-XANES measurements. X-ray absorption by Fe-bearing inclusions or

crystalline host phases that may be present within the analytical path will be mixed with the signal of the targeted glass. This is a particular problem for analyzing MI, as MI are often less than 100 μm thick. Consequently, most MI must be doubly intersected for Fe-XANES analysis to avoid signal contamination from the host mineral. A further complication in XANES measurements of MI, particularly for highly penetrative Fe-XANES analyses, is that many μXANES beamline configurations utilize a ~45° slant geometry of incoming X-ray beam in fluorescence operating modes. The inclined incidence angle means that as wafer thickness increases in the beam direction, progressively wider doubly-intersected MI areas are needed to keep the analytical path free of mineral contamination (Figure 1). Throughout the X-ray penetration volume, the minimum required doubly-intersected MI dimensions for a host-free glass measurement are roughly equal to MI thickness plus the beam diameter size (assuming a cylindrical doubly-intersected MI area). This requires MI to be either sufficiently wide or ground very thin for clean glass analyses using high energy X-rays (e.g., Fe-XANES, V-XANES, Cu-XANES). Thus, small MI in olivine and other Fe-bearing phases can be challenging to measure for Fe-XANES. Even for analyses of MI in phases that have low, but non-zero, Fe-concentrations (e.g., feldspars), the high penetrative depth of Fe-XANES can excite a large volume of the host phase, so that the host contribution to the Fe-XANES signal may be significant. This issue is of particular concern for small MI and for glass compositions with relatively low Fe-contents, such as dacites and rhyolites. At the lower energy S *K*-edge (~2500 eV), X-rays are more strongly attenuated, with the 1/e X-ray absorption depth in basaltic glass only ~5 μm. Consequently, 95% of the S-XANES X-ray absorption occurs within the upper 15 μm and most of these geometric concerns are accordingly lessened (Figure 1A).

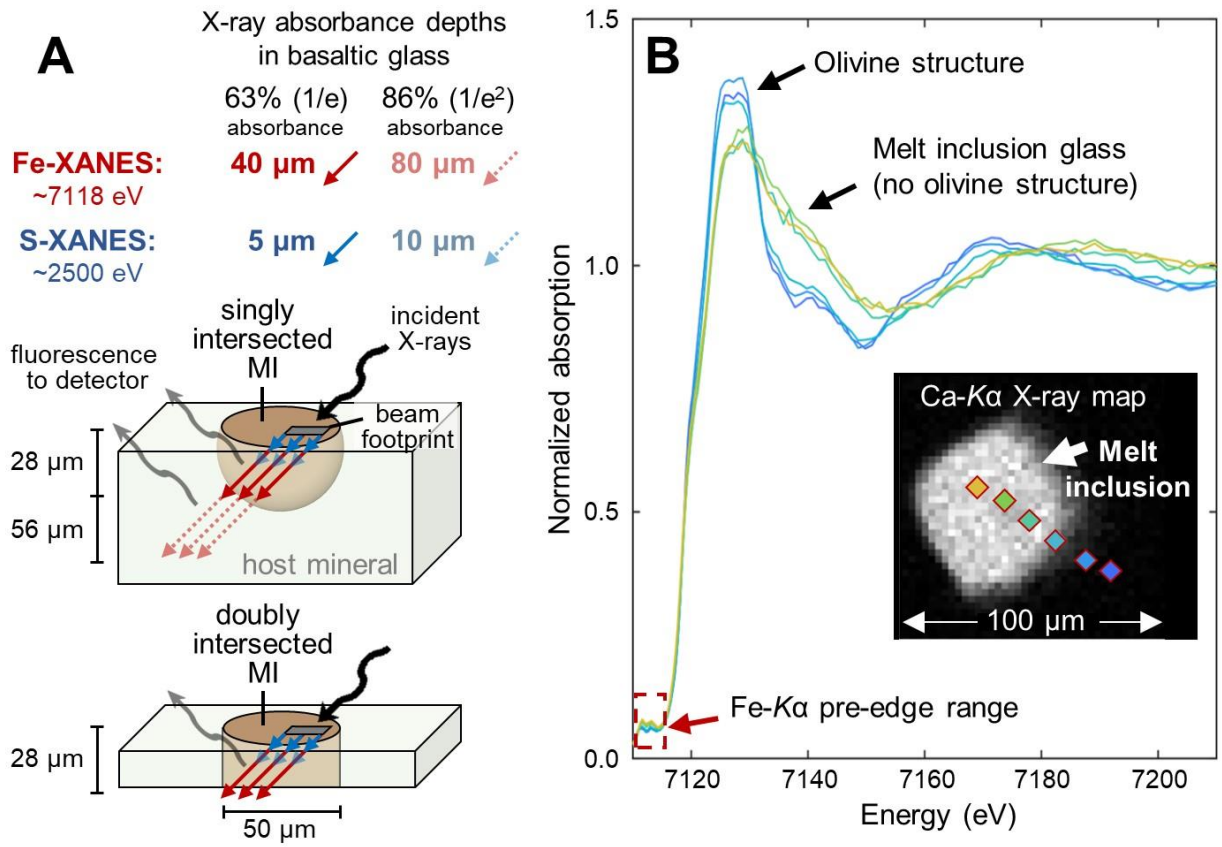


**Figure 1.** *(A)* Schematic analytical XANES geometry of a 50 µm diameter melt inclusion (MI) (brown) analyzed with a 20×20 µm X-ray beam. For many XANES fluorescence measurements, the X-ray beam (black arrow) is ~45° incident to the sample surface and the sample fluorescent energy (gray arrows) is measured at 45° in the opposite direction. Depending on the penetration depth of the X-ray energy being used, the beam may interact with substantial host mineral both laterally and at depth, leading to mineral-contaminated spectra. For Fe-XANES (red arrows), 63% and 86% of the X-ray signal are absorbed in 40 and 80 µm hypotenuse paths through basaltic glass (28 and 56 µm vertical thicknesses), requiring the MI be both doubly intersected and sufficiently wide to avoid host mineral contamination. S-XANES X-ray energies are much less penetrating (blue arrows), so MI geometry and thickness concerns are lessened. *(B)* A series of Fe-XANES measurements of a doubly-intersected olivine-hosted MI from the southern Cascades (BORG-1_37, Table 1) showing a traverse from within the MI into the olivine-host, demonstrating the difference in absorption edge shape between analyses of glass and of olivine. Measurement locations are shown atop a Ca Kα X-ray map (inset), with symbol colors matching the shown spectra.

### 2.1.2 Analytical details and sample descriptions

Fe- and S-XANES measurements were conducted on a variety of volcanic and experimental silicate glasses at GSECARS beamline 13-ID-E at Argonne National Laboratory's (Illinois, USA) Advanced Photon Source (APS), a third generation synchrotron light source

(Sutton et al., 2017). Details of the 13-ID-E beamline configuration are described in Head et al. (2018) and are consistent with measurements conducted here, except for differences in photon flux and analytical times described below.

To account for differences in monochromator calibrations between synchrotron facilities, a set of standards (minerals, metal foils, synthetic glasses) were measured at the onset of each analytical session to determine the appropriate energy offset to apply to Fe- and S-XANES oxybarometer calibration curves relative to reference energy fitting ranges (details below). At beamline 13-ID-E, the lattice constants for the monochromator Si(111) and Si(311) crystals are calculated from reference foils measured throughout the analyzable energy range of the crystals, and provide excellent consistency with absorption edge energies determined by Kraft et al. (1996). The 13-ID-E beamline has excellent reproducibility in measured reference materials over the course of standard two to three-day measurement periods and therefore no within-session drift corrections were applied during either Fe- or S-XANES measurements. Prior to each XANES analysis, an X-ray map was made by rapidly rastering across the sample to identify areas in MI and other glass targets that were free of host mineral and microlite crystals in the beam path. The X-ray beam was then turned off to prevent any further unnecessary beam interaction with the glasses until XANES measurements began.

Analyzed samples include doubly-intersected MI and matrix glasses mounted on Fe-free glass rounds and thin sections. Samples were embedded in CrystalBond®, EpoThin® epoxy, or thin section resin. All bonding material and glass substrates were analyzed to confirm that they contained only trace iron and had negligible contribution to Fe-XANES signals. The bonding materials did contain substantial S, but the low energy X-rays for S-XANES measurements are fully absorbed within a ~20 μm path within basaltic glasses (15 μm vertical path with 45º incident beam angle, Figure 1A). All analyzed MI and matrix glass areas are thicker than 20 μm, so that the bonding materials contributed no appreciable signal to S-XANES measurements. We also analyzed singly intersected experimental glass charges, where glass thicknesses of multiple mm fully absorbed X-rays at both Fe- and S-*K*α energies so that contamination from the capsule material was insignificant. In experimental glass charges, care was taken to analyze only crystal-poor glass areas and to avoid measurements near capsule edges.

259

260 **Table 1**: Experimental and natural glasses analyzed by Fe- and S-XANES in this study.

| **Sample, composition** | **$H_2O$ (wt%)** | **Fe-XANES beam damage susceptibility index (Φ)*** | **XANES analysis type** | **$Fe^{3+}/\Sigma Fe$ and $S^{6+}/\Sigma S$ ranges**** | **Photon density (photons/s/μm$^2$); observed beam damage***** |
|---|---|---|---|---|---|
| **CAB-47**: experimental basaltic glass. 1250 °C, 1.3 GPa, minor phenocrysts (Weaver et al., 2011; this study) | 5.5 | 1.6 | Fe-XANES (+ photo-oxidation time series tests) S concentration too low for S-XANES | 0.13 $Fe^{3+}$ | Fe-XANES: $1 – 1.5\times10^8$: high $2 – 4\times10^7$: high $6 – 9\times10^6$: med |
| **CAB-33**: experimental basaltic glass. 1225 °C, 1.7 GPa, phenocryst-free, but Fe-oxide nanolite spectral signature (Weaver et al., 2011; this study) | 7.2 | 1.8 | Fe-XANES (+ photo-oxidation time series tests) S concentration too low for S-XANES | Fe-oxide nanolites present | Fe-XANES: $2 – 4\times10^7$: severe $6 – 9\times10^6$: high |
| **P2-F**: Mono Craters obsidian pyroclast with <0.1% microlites (Barnes et al., 2014; Watkins et al., 2017; this study) | 2.0 – 2.3 | - | Fe photo-oxidation time series tests | - | Fe-XANES: $1 – 1.5\times10^8$: med $2 – 4\times10^7$: slight |
| **G466:** experimental basalt glass. 1300 °C, 2 GPa, minor clinopyroxene + anhydrite (Chowdhury and Dasgupta, 2019; this study) | 6.5 | - | S-XANES | 1.0 $S^{6+}$ | S-XANES: $5\times10^9$: severe $2\times10^8$: high $5\times10^7$: med $8\times10^6$: slight |
| **G479:** experimental basalt glass. 1300 °C, 1.5 GPa, minor anhydrite (Chowdhury and Dasgupta, 2019; this study) | 8.9 | - | S-XANES | 1.0 $S^{6+}$ | S-XANES: $8\times10^6$: slight |
| MORB glasses: **VG-2** (Jarosewich et al., 1980; Rose and Brown, 2017; Zhang et al., 2018; this study) **JDF-46N** (Fiege et al., 2014; this study**)** **ALV892-1** (Fiege et al., 2014; this study**)** | <0.1 | ~0.01 | S-XANES | ~0.15 $Fe^{3+}$ 0.04 – 0.08 $S^{6+}$ | S-XANES: $1\times10^{10}$: severe $4.5\times10^8$: high $1\times10^8$: med $6.5\times10^6$: slight |
| **KE62-3293S:** Kīlauea 2018 basaltic pumice MI and matrix glass (Lerner et al., 2021; this study) | 0.1 – 0.3 | 0.1 | Fe-XANES S-XANES | 0.13 – 0.18 $Fe^{3+}$ 0.03 – 0.25 $S^{6+}$ | Fe-XANES: $2 – 4\times10^7$: none S-XANES: $2\times10^8$: med $5\times10^7$: slight $8\times10^6$: none |
| **KE62-3315F:** Kīlauea 2018 littoral bomb MI and matrix glass (Lerner et al., 2021; this study) | 0.1 – 0.2 | 0.03 | Fe-XANES S-XANES | 0.20 – 0.34 $Fe^{3+}$ 0.68 – 0.96 $S^{6+}$ | Fe-XANES: $2 – 4\times10^7$: none S-XANES: $5\times10^7$: high $8\times10^6$: slight |
| Lassen (southern Cascades): olivine-hosted MI **BRM, BBL, BORG** (Muth and Wallace, 2021; this study) | 0.3 – 3.7 | 0.1 – 0.7 | Fe-XANES S-XANES | 0.14 – 0.31 $Fe^{3+}$ 0.20 – 0.98 $S^{6+}$ | Fe-XANES: $2 – 4\times10^7$: med S-XANES: $5\times10^7$: med $8\times10^6$: slight |
| Augustine 2006: **AUG_308** – low silica andesite tephra; **AUG_HSA2** – high silica andesite tephra (Lerner, 2020; this study) | 1.0 – 4.0 | 0.2 | Fe-XANES | 0.39 – 0.44 $Fe^{3+}$ (in glasses with no Fe-oxide nanolites) | Fe-XANES: $1 – 1.5\times10^8$: slight to none |
| **Cerro Negro:** olivine-hosted MI (Gaetani et al., 2012; this study) | 3.0 – 4.0 | 0.5 | Fe-XANES | Fe-oxide nanolites present | Fe-XANES: not tracked with repeat scans |

* Fe-XANES beam damage susceptibility index (Cottrell et al., 2018): $XH_2O*2XFeO/XFe_2O_3$, calculated using molar fractions and $Fe^{2+}/Fe^{3+}$ from time-zero interpolated Fe-XANES measurements. Full glass compositions are presented in the **Data supplement**.
** $Fe^{3+}/\Sigma Fe$ and $S^{6+}/\Sigma S$ ranges for beam damage corrected Fe- and S-XANES analyses. XANES spectra and results are presented in the **Data supplement.**
***Incident photon flux was ~3 – $5\times10^9$ photons/s for Fe-XANES, and ~1 – $50\times10^9$ photons/s for S-XANES. Analysis footprint sizes ranged from 2×2, 5×5, 10×10, 20×20, and 50×50 μm. Qualitative beam damage observations were based on 2 – 4 repeated scans, with total scan times of 8 – 12 minutes and 10 – 15 minutes per location for Fe- and S-XANES measurements, respectively.

## 2.2 Identifying and correcting Fe-XANES beam damage

Fe-XANES measurements were made in fluorescence mode at APS during analysis sessions in 2018 and 2019. The APS 13-ID-E beamline can deliver a focused, unattenuated X-ray beam to the sample at the Fe *K*-edge energy with a photon flux exceeding $1\times10^{12}$ photons/s. Fully focused beam sizes of ~1×2 μm are achievable, providing flux densities up to $5\times10^{11}$ photons/s/$\mu m^2$. Cottrell et al. (2018) and Moussallam et al. (2019) show that beam damage during Fe-XANES analysis scales with delivered photon dose over the measurement duration. Therefore, for the analyses presented here, photon dose was minimized during Fe-XANES analyses as follows:

1) Photon flux was attenuated using high-purity aluminum foil filters in the beam path (6 sheets of foil, totaling 222 μm thick), which decreased the incident photon flux to ~3 – $5\times10^9$ photons/s, consistent with an approach used in previous studies (Brounce et al., 2017; Moussallam et al., 2019; Tassara et al., 2020; Gaborieau et al., 2020).
2) Flux density on the sample was further decreased by defocusing the incident X-ray beam so that photon densities were generally 1 – $1.5\times10^8$, 2 – $4\times10^7$, and 6 – $9\times10^6$ photons/s/$\mu m^2$ for 5×5, 10×10, and 20×20 μm beam footprints, respectively.
3) Analysis times were minimized as much as possible while still providing interpretable spectra, which allowed us to reduce beam exposure.

The 13-ID-E monochromator calibration provides a first derivative of the Fe *K*-edge peak of iron foil at ~7110.7 eV, consistent with values determined by Kraft et al. (1996). We followed the Fe-XANES measurement methodology outlined in Head et al. (2018), but with modified scan times and energy ranges used to further identify and correct for beam damage. Two different analytical setups were used: rapid pre-edge scans and slower full energy scans. For rapid scans, the incident beam was scanned from 7092 – 7107 eV in 2.5 eV steps, from 7107 – 7119 eV in

0.1 eV steps, and from 7119 – 7144 eV in 0.05 $Å^{-1}$ (0.5 – 1.0 eV) steps (continuous steps rather than discrete). Each scan step was 0.5 seconds (s) and the total scan time was 82 s, with ~10 s delay prior to the next analysis for beamline adjustment and computational processing. The rapid pre-edge scans quickly measure over a reduced energy range to minimize beam exposure to the extent possible while still collecting spectra with high enough resolution for peak fitting in the pre-edge region. The 82 s scan is much faster than typical Fe-XANES scan durations reported in the literature, which usually range from 270 s to >700 s (4.5 to >10 minutes) (e.g., Cottrell et al., 2009, 2018; Moussallam et al., 2016; Head et al., 2018; Gaborieau et al., 2020; Tassara et al., 2020). The slower, full energy range scans measured from 7012 – 7102 eV in 2.5 eV steps, from 7102 – 7120 eV in 0.1 eV steps, and from 7120 – 7356 eV in 0.05 $Å^{-1}$ (0.5 – 3.0 eV) steps. Each scan step time was either 0.5 or 1 s and total scan durations were 176 or 352 s. This full energy range scan served as a higher-resolution scan of both the pre- and post-absorption edge regions, which is similar to analytical procedures reported in other Fe-XANES studies and allowed spectra to be normalized and assessed for mineral contamination.

Measured spectra were normalized to the incident flux (*K*α fluorescent intensity / incident flux [I0]) and were fit using XAS viewer within the LARCH software package (Newville, 2013). $Fe^{3+}/\Sigma Fe$ was calculated using relative pre-edge peak intensities following approaches described in Cottrell et al. (2009). This approach uses the calculated centroid energy of the pre-edge doublet, which is related to the 1s → 3d electron transition, to determine glass $Fe^{3+}/\Sigma Fe$ based on calibrations to standard glasses equilibrated at known $fO_2$ conditions and measured using Mössbauer spectroscopy (Berry et al., 2003; Wilke et al., 2004; Cottrell et al., 2009). An energy offset between our basaltic glass measurements and those used in the Fe-XANES calibration of Cottrell et al. (2009) (due to monochromator calibrations and background subtractions during peak fitting) was determined by comparing the Fe pre-edge centroid position of basaltic reference glass LW_0 (Cottrell et al., 2009, 2018; Zhang et al., 2016, 2018) from the Smithsonian Institution. The split of LW_0 glass analyzed here is embedded in the mount NMNH 118279/IGSN NHB007V34, and is the same specimen as found in the mount with catalog number NMNH 117393/IGSN NHB0073V8 (both available by request from the Smithsonian Institution). The pre-edge centroid position of LW_0 was measured by Cottrell et al. (2009) to have an energy of 7112.30 eV using the beamline configuration they described at the National Synchrotron Light Source (Brookhaven National Laboratory). All Fe-XANES

spectra in figures and data tables throughout this manuscript are presented in energy units as-measured at APS. However, when calculating iron valences in basaltic glasses, energy shifts of +0.317 and +0.323 eV were respectively applied to iron pre-edge centroid positions for measurement sessions 2018-3 and 2019-2 to provide consistency with centroid values measured for LW_0 in Cottrell et al. (2009). Pre-edge peak fitting ranges were similarly adjusted from Cottrell et al. (2009) to span an energy range of 7108.7 – 7116.7 eV, consistent with the methodology discussed in Zhang et al. (2016). Within this fit window, the absorption baseline of the main Fe *K* absorption edge was fit using a linear and a Lorentzian function, and the pre-edge doublet was fit using two Gaussian functions (Cottrell et al., 2009). The centroid value of the these two peaks was used to calculate $Fe^{3+}/\Sigma Fe$ using the Mössbauer-based calibration of Zhang et al. (2018) for basaltic glasses.

For dacitic and rhyolitic glasses, average iron valence was calculated from a parameterization of Fiege et al. (2017) for felsic glasses. No energy offsets were applied because our measurements of the first derivative of the absorption edge of iron foil were consistent with those of Fiege et al. (2017). Uncertainties in centroid values (±1 SE), as detailed below, are propagated through the basalt or rhyolitic calibrations to calculate uncertainties of $Fe^{3+}/\Sigma Fe$ calculations.

### 2.2.1 Timescales of Fe-XANES beam damage

Fe-XANES analysis of hydrous silicate glasses with a high intensity X-ray beam can cause rapid photo-oxidation of $Fe^{2+}$ to $Fe^{3+}$ within the glass, creating large inaccuracies in determining the initial $Fe^{3+}/\Sigma Fe$ values of glasses (Cottrell et al., 2018; Moussallam et al., 2019) (Figure 2). The extent of this oxidation varies depending on glass composition and photon dose. Beam-induced oxidation causes a shift in Fe-*K*α pre-edge peak intensities but does not produce any uniquely identifiable spectral features. Consequently, it is impossible to know from a single Fe-XANES analysis whether a sample had suffered from beam-induced photo-oxidation (compare with S-XANES beam damage, which produced diagnostic spectral features, as discussed in section 2.3). Therefore, samples must either be analyzed under carefully tested analytical conditions to ensure that no significant beam damage occurs for the particular glass composition and analysis duration, or a method must be employed that can identify and correct for beam damage in each individual analysis spot. We emphasize the latter approach in this

study, presenting a method that allows us to reliably analyze small, hydrous glass inclusions with a relatively high-flux beam.

To identify and correct for beam damage within each analysis spot, we conducted multiple rapid scans of the Fe *K* pre-edge region to create a time series of progressive oxidation (Figure 2). These time series allow us to assess whether beam damage occurred during analysis and, if needed, enables us to calculate sample-specific corrections. For each analysis spot, we conducted 3 to 6 rapid pre-edge scans (82 s) followed by one full energy scan (176 or 352 s) across the entire Fe *K* absorption edge energy range. If pre-edge centroids calculated from the rapid scans did not show progressive oxidation over time, the spectra were merged together to form a single higher-resolution pre-edge spectrum. If changes in pre-edge centroid positions were observed, we use the time series of centroid positions to extrapolate the centroid back to t=0 s. We take this extrapolated value as the initial, 'correct' centroid position prior to beam exposure. This time-dependent correction approach is similar to methods commonly applied to electron microprobe measurements to account for alkali migration during electron beam excitement (Kuehn et al., 2011). A time-dependent approach has also been recently proposed for determining iron valence by electron microprobe measurements (Hughes et al., 2018).

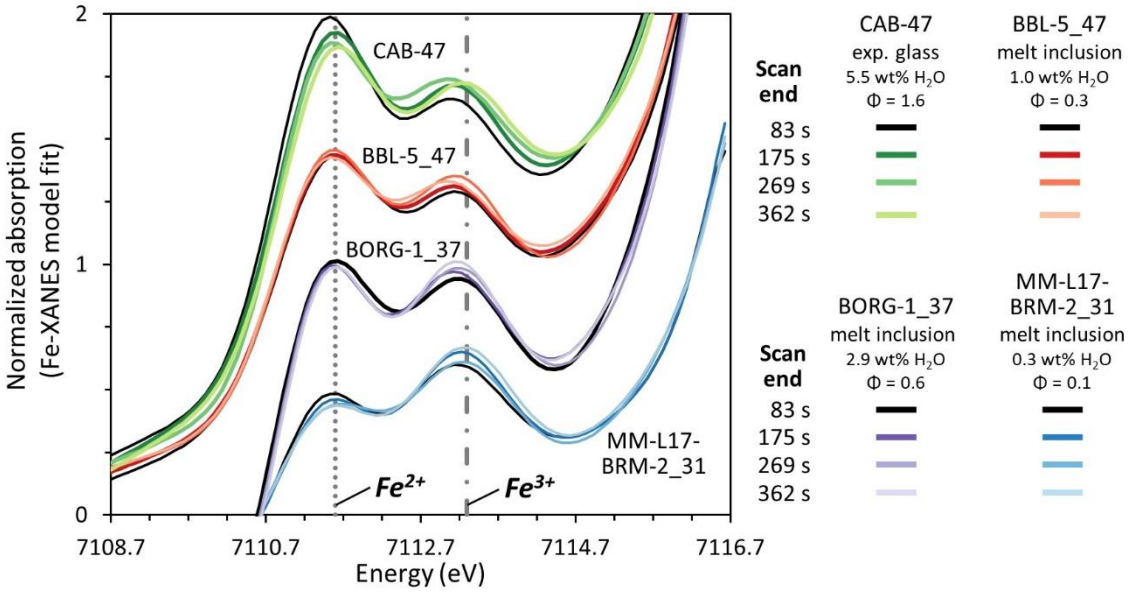


**Figure 2**. Model fits to Fe-XANES pre-edge spectra for repeated rapid scans of experimental basaltic glass CAB-47 and of melt inclusions from the southern Cascades (CA, USA). Spectra of different samples have been vertically shifted for clarity. Progressive oxidation occurs during repeated rapid scans, as evidenced by the lighter colored lines. Samples have different initial

$Fe^{3+}/\Sigma Fe$ and $H_2O$ contents, which affect the extent of beam-induced photo-oxidation. Measurements were made with a 10×10 μm beam and photon flux densities ranged from 2 – $4\times10^7$ photons/s/$\mu m^2$. The lines labeled $Fe^{2+}$ and $Fe^{3+}$ refer to the approximate positions of the first and second pre-edge doublet peaks.

X-ray induced photo-oxidation during Fe-XANES analysis can be difficult to identify, partly because a large extent of the valence change occurs rapidly in the first minutes of analysis (Cottrell et al., 2018; Moussallam et al., 2019). To ensure that our sequences of repeated rapid scans adequately captured changes to centroid positions during the earliest stages of photo-oxidation, we measured changes to the intensity of the 2nd pre-edge doublet (at 7113.2 – 7113.4 eV at APS) in single spots over 6 – 16 minutes. Such dwell tests measure the photo-oxidation of the analyzed glass at a much finer temporal resolution than pre-edge scans allow (Shorttle et al., 2015; Cottrell et al., 2018; Moussallam et al., 2019; Gaborieau et al., 2020). However, one limitation to such single-energy dwell tests are that other simultaneously changing spectral features cannot be detected. Additionally, one must assume that any changes in spectral background during the measurement duration are negligible.

We conducted a set of dwell tests on an experimental basaltic glass (CAB-47, Weaver et al. [2011]) (Figure 3A, B) with a high $H_2O$ content (5.5 wt%) and a high proportion of $Fe^{2+}$ (~0.13 $Fe^{3+}/\Sigma Fe$). Sample CAB-47 shows larger degrees of beam-induced oxidation of iron compared to the natural glasses studied here, likely due to its combined high $H_2O$ and $Fe^{2+}$ contents (Cottrell et al. 2018). The calculated beam damage susceptibility index ($\Phi$, where $\Phi = XHO_{0.5} * XFeO/XFeO_{1.5}$), as described in Cottrell et al. (2018), is 1.6 for CAB-47 compared to $\Phi$ of 0.1 – 0.7 for the various natural MI investigated in this study (Figure 5, Table 1). We therefore use this highly beam damage-susceptible experimental glass to evaluate models for correcting changing iron valence during Fe-XANES analysis.

To evaluate if time series of repeated rapid pre-edge scans (82 s durations, described above) are sufficiently fast to capture photo-oxidation in CAB-47, we compared the pre-edge rapid scan time series to the 2nd pre-edge doublet dwell tests in the same glass (Figure 3, Figure A.1). It is assumed that the rate of change of the 2nd pre-edge doublet intensity scales with the change in centroid value during time series analyses (Cottrell et al., 2018; Moussallam et al., 2019). Dwell tests of the 2nd pre-edge doublet of CAB-47 with a photon flux density of ~$1.4\times10^8$ photons/s/$\mu m^2$ (analyzed with a 5×5 μm spot size) show that substantial photo-oxidation occurs

in the first minute of analysis, with $Fe^{3+}/\Sigma Fe$ increasing from 0.13 to 0.19. Under these high photon flux densities, photo-oxidation progresses non-linearly (Cottrell et al., 2018; Moussallam et al., 2019; Figure 3, Figure A.1). The time series of repeated rapid pre-edge scans cannot capture this non-linear behavior that occurs in the initial 10s of seconds of analysis, and therefore cannot adequately characterize photo-oxidation at such high photon flux densities (Figure 3A, C). However, by decreasing the photon flux density to ~$4.3\times10^7$ photons/s/μm$^2$ (using a 10×10 μm spot size), dwell tests of CAB-47 show that photo-oxidation is slow enough that changes to both the 2nd pre-edge doublet intensity and centroid values can be adequately approximated by fitting a linear function to repeated rapid pre-edge scans (Figure 3B, D). Although photo-oxidation may remain non-linear in the initial minute of analysis even at this lower photon dose, the linear fit approximates the data within typical measurement uncertainty and is thus a reasonable approximation. The progression of photo-oxidation becomes more linear with further decreased photon flux densities (Figure A.1).

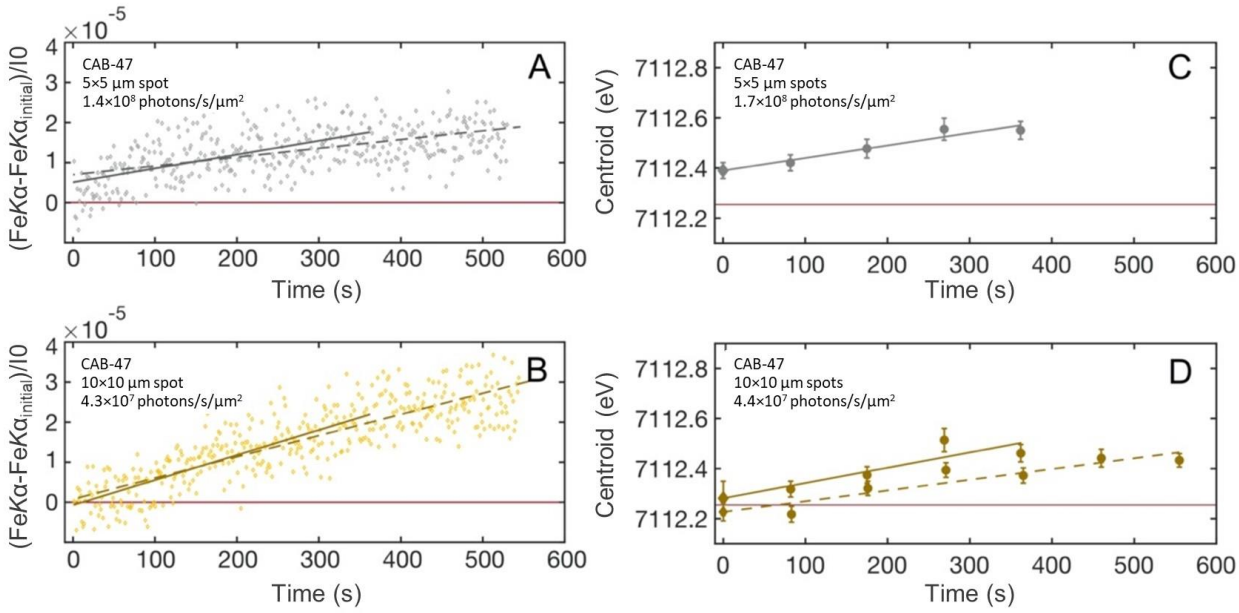


**Figure 3**. *(A, B)* Intensities of the 2nd pre-edge doublet as a function of time in experimental glass CAB-47 measured with photon flux densities of $1.4\times10^8$ and $4.3\times10^7$ photons/s/μm$^2$ (5×5 μm and 10×10 μm respective spot sizes). Gray and yellow lines are linear regressions through data from 0 to 362 s (solid) or 0 to 537 s (dashed). Fe-*K*α/I0 initial intensity (red horizontal line) is taken as the average of the first 5 analyses. *(C, D)* Pre-edge centroid positions calculated from repeated rapid scans (see Figure 2) for experimental glass CAB-47 with photon flux densities of $1.7\times10^8$ photons/s/μm$^2$ (5×5 μm spot size; one time series) and ~$4.4\times10^7$ photons/s/μm$^2$ (10×10 μm spot size; two time series). Each circle is a centroid value calculated from one pre-edge scan

with error bars representing ±1 SE of centroid fits to each scan. Diamonds at t=0 s are the intercept of linear regressions to each time series and are taken to be beam damage corrected centroid values. Error bars on the t=0 s centroid positions represent ±1 SE of the time series linear regression. Red lines in panels *C* and *D* are the estimated initial centroid value, which is taken as the average beam damage corrected centroid values for the two 10×10 μm analysis time series (panel *D*). Gray and yellow lines are linear regressions through centroid values from 82 to 362 s (solid) or 82 to 537 s (dashed). Centroid values in *C* and *D* have been shifted by +0.32 eV for consistency with the LW_0 centroid position reported by Cottrell et al. (2009).

The same dwell tests were conducted using similar photon densities on another experimental hydrous basaltic glass (CAB-33, 7.2 wt% $H_2O$, $\Phi$ = 1.8; Weaver et al., 2011) and on a moderately hydrous natural obsidian pyroclast from Mono-Inyo Craters (CA, USA) (P2-F, ~2.2 wt% $H_2O$; Barnes et al., 2014; Watkins et al., 2017; Table 1) Observed changes to the 2$^{nd}$ pre-edge doublet intensity in these glasses were similar to those measured in CAB-47 (Figure A.1), suggesting that the time series correction approach can be applied across a range of basalt to rhyolite glass compositions, including hydrous samples that are highly susceptible to photo-oxidation.

### 2.2.2 Applying the Fe-XANES beam damage correction technique to natural melt inclusions

Because glass CAB-47 is more susceptible to beam damage than most MI and matrix glasses, changes to pre-edge centroids in most natural samples analyzed under the same conditions (~$3.0\times10^7$ photons/s/μm$^2$) can also be approximated with a linear function. Hydrous basaltic MI from the southern Cascades arc (0.3 – 3.7 wt% $H_2O$, $\Phi$ = 0.1 – 0.7) show consistent increases in pre-edge centroid values over the course of several repeated rapid scans, indicating progressive photo-oxidation (Figure 4, Table 1). In contrast, basaltic MI from Kīlauea Volcano (HI, USA) do not show time-dependent changes to pre-edge centroid values, as expected based on their low $H_2O$ contents and low beam damage susceptibilities (0.1 – 0.3 wt% $H_2O$, $\Phi \leq 0.1$) (Figure 4, Table 1). The slopes of linear regressions to centroid time series (i.e., the rate of photo-oxidation) are inversely correlated with calculated initial $Fe^{3+}/\Sigma Fe$ and are positively correlated with $H_2O$ contents of each glass (Figure 5, Figure A.2). These observations are consistent with beam damage occurring more readily in reduced and/or hydrous glasses (Blundy et al., 2020; Cottrell et al., 2018).

To apply time series corrections in beam damage-susceptible samples, linear regressions using 4 rapid pre-edge scans are generally sufficient to correct to initial (t=0 s) centroid positions. However, using up to 6 pre-edge scans can provide an improved regression fit, as increased scans minimize the leverage of anomalously noisy scans in the regression (Figure 3D). Uncertainties in restored initial centroid positions were assessed by calculating the standard error of regression for each time series and by calculating the standard deviation of time series linear fits using a Monte Carlo method that incorporates the standard error of each individual centroid fit (Browaeys, 2021). For the analytical conditions used in this study, these two approaches yield similar uncertainty estimates for the t=0 s centroid positions (Figure A.3). Weighting the linear regressions by the inverse of the squared standard deviation of each measurement's uncertainty also yields similar linear fits and standard error estimates for t=0 s centroid values. In time series with substantial scatter in centroid positions, the standard error of linear regressions is generally larger than the Monte Carlo-derived uncertainty estimates (Figure A.3). We therefore use the standard error of unweighted linear regressions to estimate uncertainties in the restored t=0 s centroid positions, as this is the simplest and generally most conservative approach.

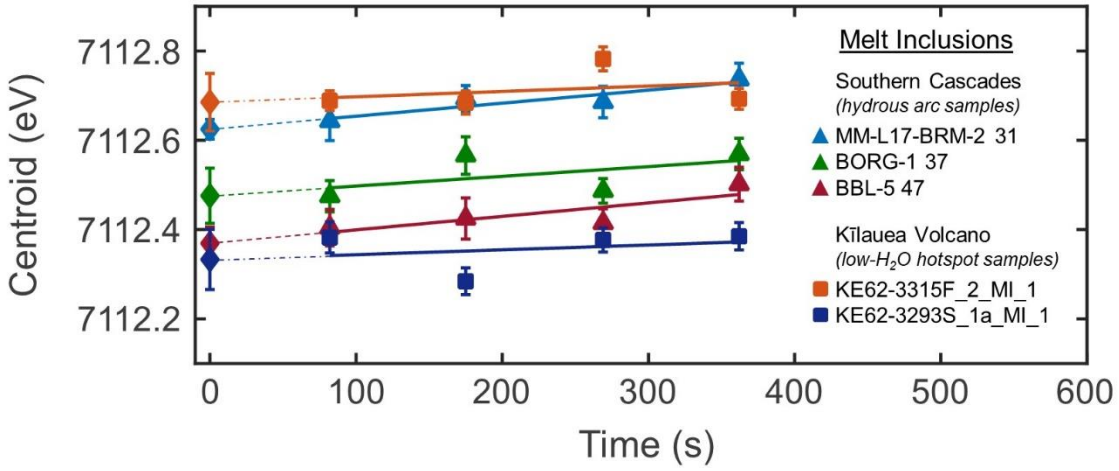


**Figure 4.** Fe *K*α pre-edge centroid positions calculated from repeated rapid scans of MI from the southern Cascades (triangles) and from Kīlauea Volcano (squares). Symbols are the centroid values calculated from individual pre-edge scans and error bars represent ±1 SE for each centroid fit. Lines are linear regressions through centroid values from 82 to 362 s. Diamonds at t=0 s are the intercept of each regression (dashed lines), taken to be the beam damage corrected centroid position. Error bars on diamonds represent ±1 SE of the time series linear regression. Analyses used a 10×10 μm spot size, which resulted in photon flux densities of $3 – 5\times10^7$ photons/s/μm$^2$.

All centroids have been shifted by +0.32 eV for consistency with the LW_0 centroid position reported by Cottrell et al. (2009).

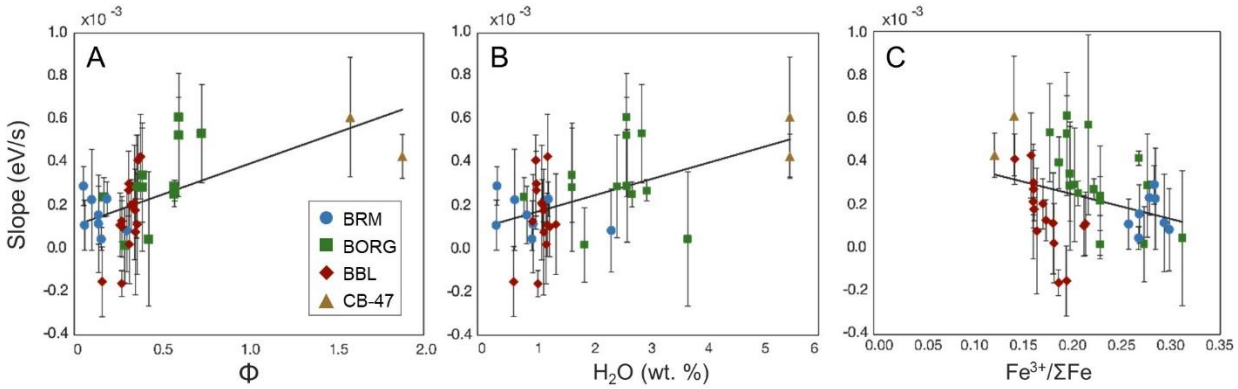


**Figure 5.** Slopes of linear regressions through centroid value time series for individual glasses plotted as a function of *(A)* beam damage susceptibility index ($\Phi = XHO_{0.5} * XFeO/FeO_{1.5}$) as defined in Cottrell et al. (2018), *(B)* $H_2O$ content, and *(C)* initial $Fe^{3+}/\Sigma Fe$. Melt inclusions from southern Cascades cinder cones (BORG, BRM, BBL) and experimental glass analyses (CAB-47) are grouped by color. Gray lines are linear regressions through analysis spots from all natural and experimental samples.

For hydrous basaltic MI from the southern Cascades, the average 1 standard error of regression for corrected t=0 s centroid values is ±0.04 eV, or ±0.02 $Fe^{3+}/\Sigma Fe$ when propagated through the calibration of Zhang et al. (2018) (note that curvature of the calibration function increases $Fe^{3+}/\Sigma Fe$ uncertainties in more oxidized glasses). This uncertainty is only slightly larger than the average standard error of centroid value fits of our higher resolution full length scans (±0.03 eV; ±0.01 $Fe^{3+}/\Sigma Fe$), and is much smaller than the ~0.15 variation in $Fe^{3+}/\Sigma Fe$ measured in basaltic arc MI globally (Kelley and Cottrell, 2009; Brounce et al., 2014; Muth and Wallace, 2021). Regressions on replicate analyses within the same MI yield corrected centroid positions that are within error of each other (Figure A.4), indicating that our correction approach is reasonably accurate.

### 2.2.3 Discussion and summary

Although the time-dependent beam damage correction approach introduces some imprecision, it ensures that data sets are not systematically biased to higher calculated $Fe^{3+}/\Sigma Fe$ values due to uncorrected photo-oxidation. In analyses of basaltic MI from the southern Cascades (measured with photon flux densities of $1 – 5\times10^7$ photons/μm/s$^2$), the difference

between corrected and uncorrected centroid positions is large (Figure 6). On average, centroid values measured after 362 s of analysis are 0.09 eV higher than t=0 s corrected centroid values. This means that despite measures taken to lower the photon flux, had we analyzed these hydrous MI with more typical 10-minute duration scans (where the pre-edge region is measured within the first ~6 minutes) our analyses would have overestimated melt $Fe^{3+}/\Sigma Fe$ by ~0.036. This would correspond to an overestimation of the $fO_2$ by 0.5 log units for basalt at 1150 °C and 400 MPa, according to the model of Kress and Carmichael (1991).

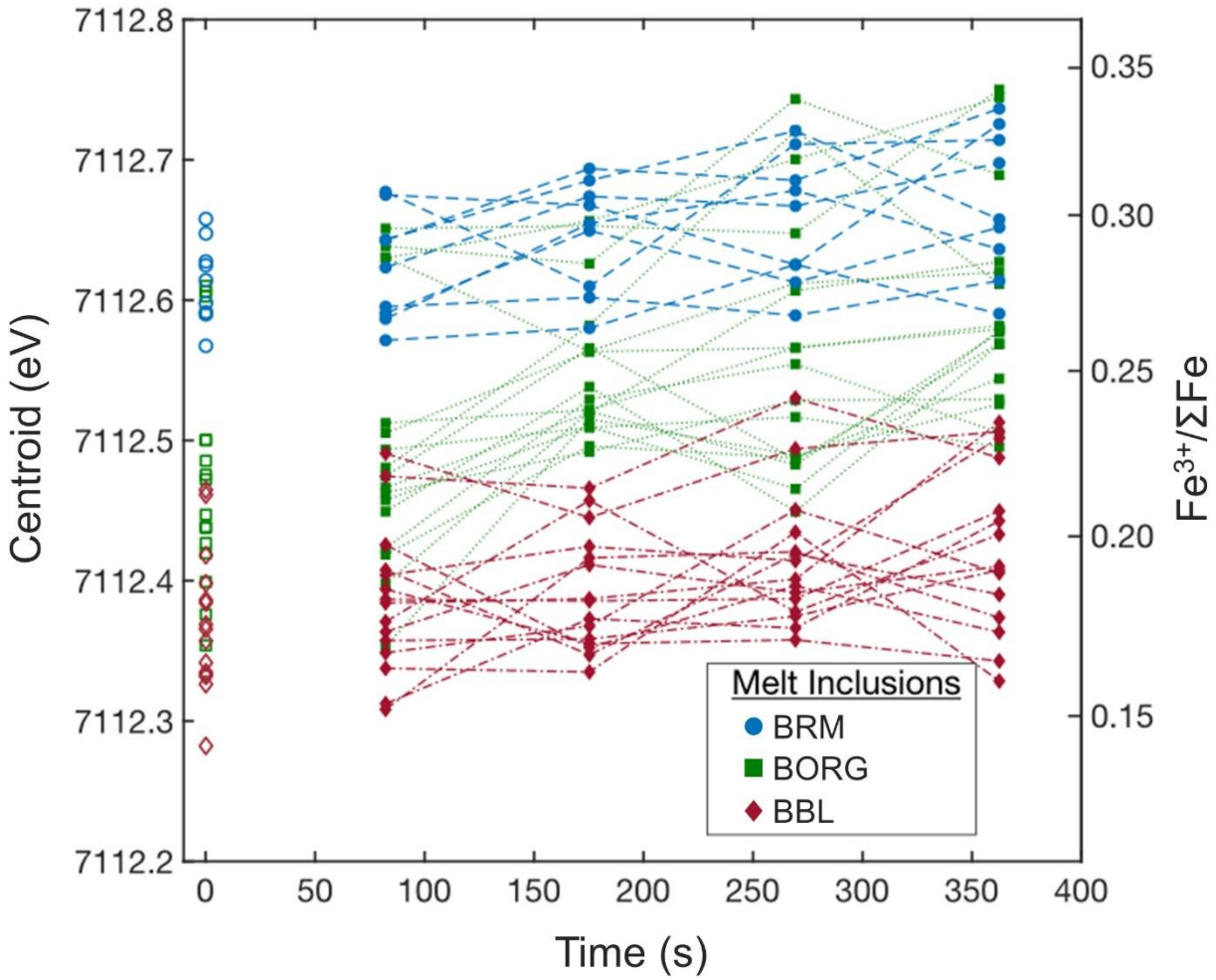


**Figure 6.** Fe-*Kα* pre-edge centroid positions through time calculated from repeated pre-edge scans for individual southern Cascades MI. Dashed lines connect centroids calculated from four consecutive rapid scans of the same analysis spot, and open symbols at t=0 s are the corrected initial centroids. Centroid time series measurements are plotted at the end time of each scan. Right vertical axis is the calculated $Fe^{3+}/\Sigma Fe$ from centroid values using the calibration of Zhang

et al. (2018). All centroids have been shifted by +0.32 eV for consistency with the LW_0 centroid position reported by Cottrell et al. (2009).

In summary, photo-oxidation during Fe-XANES measurements can cause large systematic biases toward higher calculated $Fe^{3+}/\Sigma Fe$ in beam-sensitive glasses, which can significantly affect geologic interpretations of redox conditions (Cottrell et al., 2018; Moussallam et al., 2019). Taking measures to mitigate beam damage through reduced X-ray flux density (where possible) and/or by applying analysis-specific time-dependent corrections described here is critical for accurate interpretation of Fe-XANES measurements in beam-sensitive glasses, such as hydrous arc basalts. We present a time-dependent correction method and set of analysis conditions that should enable beam damage identification and correction in most natural silicate glasses at even relatively high photon flux densities ($10^7$ –$10^8$ photons/s/$\mu m^2$). However, photo-oxidation during analysis is a function of glass composition (including $H_2O$ content and initial $Fe^{3+}/\Sigma Fe$), photon flux density, and duration of analysis, and therefore depends on the specific sample and beamline properties. Best practices during Fe-XANES analysis of glasses would include explicitly testing (via 2$^{nd}$ pre-edge multiplet dwell tests) whether repeated rapid pre-edge scans sufficiently correct photo-oxidation for the particular beamline conditions and sample composition being analyzed.

### 2.3 Identifying and correcting S-XANES beam damage

S-XANES measurements use lower X-ray energies than Fe-XANES (~2480 eV vs ~7110 eV, respectively) and therefore have smaller absorption lengths than Fe-XANES measurements. At S-XANES energies, 95% of X-ray energy is absorbed within the upper ~15 μm of glass (Wilke et al., 2011) (Figure 1A). The MI analyzed here are thicker than 15 μm so that doubly intersecting the inclusions was not necessary for S-XANES analyses. Additionally, most host minerals contain negligible sulfur compared to MI (Callegaro et al., 2020) so that beam overlap of the host mineral is less of a concern than for Fe-XANES analyses, where iron signal contribution from the host phase can be significant. Consequently, larger X-ray analysis footprints can generally be used for S-XANES, which reduces X-ray dose and thereby ameliorates some of the beam damage potential. However, when analyzing sulfur-poor MI (<~400 ppm S), even slight contributions from the host phase might be significant relative to the

low-sulfur glass signal, and beam overlap of the host phase should be avoided. Additionally, cracks and surface contaminants (e.g., oils) may be present on prepared surfaces, both of which can contain undesired sulfur-bearing material (Brounce et al., 2019). Consequently, smaller beam footprints for S-XANES remain more versatile for analysis of MI (particularly for low-sulfur samples) because of the ability to avoid contamination from host minerals or from surface aberrations.

Sulfur in silicate melts occurs as $S^{2-}$ (sulfide complexes) or $S^{6+}$ (sulfate complexes; $S^{(VI+)}O_4^{2-}$) but does not naturally occur as $S^{4+}$ (sulfite complexes; $S^{(IV+)}O_3^{2-}$) at the limit of detection by XANES (Backnaes et al., 2008; Wilke et al., 2008, 2011). The main absorption peak of $S^{2-}$ complexes in glasses occurs over a broad energy range centered at ~2476 eV, and the absorption peak of $S^{6+}$ complexes occurs at ~2482 eV (Li et al., 1995; Paris et al., 2001; Bonnin-Mosbah et al., 2002; Wilke et al., 2008; Métrich et al., 2009; Jugo et al., 2010). In Fe-bearing natural glasses, S-XANES beam damage typically manifests as photo-reduction of $S^{6+}$ to $S^{4+}$ (Wilke et al., 2008). The absorption peak for sulfite occurs at 2477.5 eV (note that the rapid oxidation of sulfite at the surface causes a 2482 eV sulfate peak to also be present in the spectra of most sulfite reference materials) (Métrich et al., 2002, 2009; Bonnin-Mosbah et al., 2002; Fleet et al., 2005; Wilke et al., 2008; Jugo et al., 2010). The 2477.5 eV sulfite peak is a unique spectral signal to recognize $S^{4+}$ speciation and thereby can be used to identify measurements that have undergone beam damage (Wilke et al., 2008; Métrich et al., 2009; Moussallam et al., 2014). Beam damage is therefore more easily detected in S-XANES than in Fe-XANES, and time-dependent corrections to t=0 s are not necessary because all observed $S^{4+}$ is generally attributable to beam-induced reduction of sulfur. Photo-reduction of $S^{6+}$ has also been observed during electron microprobe (EPMA) S-*K*α wavelength scans (Wilke et al., 2008). However, photo-oxidation of $S^{2-}$ to $S^{4+}$ or to $S^{6+}$ has been documented by other EPMA studies (Wallace and Carmichael, 1994; Rowe et al., 2007) and during extremely long duration XANES measurements (20 – 80 minutes) of highly alkalic glasses from Mt. Erebus (Antarctica) (Moussallam et al., 2014). The predominance of sulfur photo-reduction during XANES analyses of natural glasses suggests that different mechanisms of sulfur beam damage may occur under electron bombardment compared to X-ray irradiation, and potentially also during X-ray irradiation of alkali-rich glasses (Hughes et al., 2020).

The parameters influencing photo-reduction ($S^{6+}$ to $S^{4+}$) in silicate glasses during S-XANES irradiation are imprecisely known. In contrast to Fe-XANES beam damage (Cottrell et al., 2018), $H_2O$ content does not appear to be a critical control on S-XANES beam damage (see section **2.3.3**), and the compositional dependence of S-XANES beam damage susceptibility has not been thoroughly examined. It is consequently difficult to currently predict whether any particular sample will be susceptible to S-XANES beam damage. Therefore, as with iron beam damage, it is important to be able to account for beam damage within each individual measurement rather than applying generalized corrections to an entire sample suite.

Our approach in managing and correcting S-XANES beam damage is similar to that for reducing Fe-XANES beam damage, namely minimizing pre-analysis X-ray irradiation, decreasing photon dose as much as possible while maintaining sufficient signal, and using repeat rapid scans to observe beam-induced changes in sulfur speciation. Where S-XANES photo-reduction is observed, we correct affected spectra by calculating the peak area of the beam damage-induced $S^{4+}$ signal and restoring this to original $S^{6+}$ intensity via a calibrated conversion factor (details below).

### 2.3.1 S-XANES analytical conditions

S-XANES measurements at APS GSECARS beamline 13-ID-E were conducted in fluorescence mode and within a He-environment to minimize atmospheric absorption of the X-ray fluorescent signal. Incident beam flux ranged from ~$1 – 50\times10^9$ photons/s for S-XANES analyses, which was purposely lowered from the maximum possible flux to reduce rates of beam damage. Repeat measurements of sulfate within Scotch® tape during four analytical sessions between 2017 – 2020 indicate a consistent $S^{6+}$ peak position of 2481.8 eV. The sulfate peak position in crystalline hauyne measured by Jugo et al. (2010) at the European Synchrotron Radiation Facility's beamline ID21 is +1 eV relative to sulfate measurements at APS beamline 13-ID-E, due to differences in monochromator calibration (Head et al., 2018). Thus, all the Jugo et al. (2010) values presented in figures and data tables have been shifted by -1 eV for consistency.

As with our Fe-XANES beam damage correction approach, we conducted repeat rapid scans to identify S-XANES beam damage and, if necessary, applied sample-specific corrections. Sulfur *K*-edge spectra were collected by scanning the incident beam from 2437 – 2467 eV in 2.5

eV steps, from 2467 – 2487 eV in 0.1 eV steps, and from 2487 – 2622 eV in 1.5 eV steps. Short analysis times of either 0.5 or 1.0 s per step bin were used (continuous steps rather than discrete) for rapid scans with total durations of 154 or 308 s, respectively. Three repeat scans were typically conducted for each analysis spot, with cumulative measurement times of ~8 – 15 minutes per location. If $S^{4+}$ peak growth was identified during successive scans, only the first scan was used to quantify sulfur speciation, as this scan would have undergone the least $S^{6+}$ to $S^{4+}$ photo-reductive beam damage. If no $S^{4+}$ peak ingrowth was observed, the repeat scans were merged to improve signal quality.

In beam-damaged samples, $S^{6+}$ to $S^{4+}$ photo-reduction can be corrected by restoring the $S^{4+}$ 2477.5 eV peak intensity back to a $S^{6+}$ signal. This correction requires knowing an appropriate signal intensity scaling factor to restore a $S^{4+}$ signal to the original $S^{6+}$ intensity. Konecke et al. (2017) and Nash et al. (2019) apply S-XANES beam damage corrections by assuming a 1:1 intensity scaling between $S^{4+}$ and $S^{6+}$ peaks. However, in the absence of direct evidence, the accuracy of this assumed 1:1 scaling relationship of fluorescent energy outputs is uncertain. To determine how the loss of $S^{6+}$ intensity relates to the growth of $S^{4+}$, and therefore how to calculate an appropriate signal intensity scaling factor between these peak intensities, we conducted a series of measurements on a hydrous, sulfate-dominated, sulfur-rich experimental basaltic glasses from Chowdury and Dasgupta (2019) (Table 1). The large area of this experimental glass allowed a series of measurements with multiple spot sizes (2×2, 10×10, 20×20, and 50×50 μm) to observe varying degrees of beam damage under photon densities ranging from $6.9\times10^{6}$ – $1.1\times10^{10}$ photons/s/μm$^2$. The sulfate-only initial composition of this oxidized glass made the identification of $S^{4+}$ peak ingrowth obvious. With repeat measurements, we are able to track the ingrowth of the $S^{4+}$ 2477.5 eV peak (hereafter the "$S^{4+}$ peak") at the expense of the $S^{6+}$ 2481.3 – 2482 eV peak. We can thereby quantify how the $S^{4+}$ peak intensity relates to the loss of $S^{6+}$ intensity, and how consistent the $S^{4+}$ to $S^{6+}$ intensity scaling relationship is with increasing degrees of beam damage.

### 2.3.2 Quantifying S-XANES spectra via peak fitting

Determining the relationship between $S^{4+}$ signal growth and $S^{6+}$ signal loss during S-XANES beam damage requires a consistent peak fitting method to quantify the change in absorption intensities. Peak fitting approaches to S-XANES spectra have been employed by

other researchers (Manceau and Nagy, 2012; Konecke et al., 2017; Nash et al., 2019), but have not been described or calibrated in silicate glasses at the level of detail required to be fully reproducible. We therefore establish a new peak fitting calibration based on the dataset used by Jugo et al. (2010) to originally define a calibration relating S-XANES signal intensities to sulfur speciation. S-XANES spectra of silicate glasses are produced by a mixture of X-ray photon absorptions by $S^{2-}$, $S^{4+}$, and $S^{6+}$ species, and by $S^{1-}$ and $S^{2-}$ sulfide complexes (Paris et al., 2001; Fleet et al., 2005; Métrich et al., 2009). Jugo et al. (2010) empirically determined a relationship of $S^{2-}$ and $S^{6+}$ X-ray absorption intensities to sulfur speciation using a set of experimental glasses by integrating all signal within energy ranges relating to $S^{2-}$ and $S^{6+}$ peaks (2474.7 – 2479 eV and 2480.5 – 2483 eV, respectively; Jugo et al. [2010] ranges have been shifted by -1 eV). However, the $S^{4+}$ absorption peak (2476.8 – 2477.6 eV) occurs within the broad $S^{2-}$ energy range. Consequently, the Jugo et al. (2010) approach would inappropriately include any photo-reduction induced $S^{4+}$ signal intensity as $S^{2-}$ intensity. Our peak fitting approach differentiates $S^{2-}$, $S^{4+}$, and $S^{6+}$ absorption intensities, enabling us to quantify beam damage by isolating $S^{4+}$ from the $S^{2-}$ peak. We can then restore the $S^{4+}$ photo-reduction signal to an original $S^{6+}$ intensity to calculate the undamaged sulfur speciation of the glass.

Our S-XANES peak fitting method again uses the spectral fitting program XAS viewer (Newville, 2013) to correct for instrument deadtime and to fit the S-XANES data. Measured spectra were first scaled by the Si-*Kα* signal intensity, to avoid aberrations in incident beam intensity over the analysis energy range due to possible contaminants within the beamline optics. Following the approach of Jugo et al. (2010) and Anzures et al. (2020), we then normalize each spectrum so that the energy range containing pre-edge features begins at zero intensity (~2467 eV), and the post-edge signal intensity is 1 (>2510 eV). This is done by defining a linear relation in the low energy range (~2441 – 2467 eV), and flattening the high energy range (~2525 – 2611 eV) to scale the spectra to between 0 – 1 (Ravel and Newville, 2005; Anzures et al., 2020). These energy ranges for normalization are guidelines that should be slightly modified as necessary if anomalous data points are present for particular scans. However, sulfide X-ray absorption begin at energies just above 2467, so the pre-edge normalization range should be kept below this energy. The normalized post-edge spectrum is fit using an error function and a broad Gaussian, which together define the background. The center point of the error function is fixed and the

width of the high-energy Gaussian is constrained to maintain a consistent background fitting approach for all spectra (Table 2).

Assessing S-XANES spectra of >100 reduced and oxidized glass analyses across a compositional range from basaltic to rhyolitic (Table 1; **Data supplement**), we identify the energy ranges of five peaks within the S-*K*α absorption region. We distinguish four absorption peak ranges that have been recognized as corresponding to sulfide complexes, and $S^{2-}$, $S^{4+}$, and $S^{6+}$ species (Wilke et al., 2008, 2011; Métrich et al., 2009; Jugo et al., 2010; Head et al., 2018) (Table 2). We additionally identify an absorption peak between 2483.5 – 2486 eV, which is slightly higher energy than the main $S^{6+}$ peak. This 2483.5 – 2486 eV energy peak was similarly identified by Konecke et al. (2017), who refer to it as the sulfur "ionization peak", a term we adopt here. The sulfur-ionization peak intensity seems partially correlated to $S^{6+}$ intensity, but is also present in $S^{2-}$-dominated spectra. After normalizing the spectra, we simultaneously fit the background with an error function and Gaussian and fit five separate Gaussian functions for each of the sulfur absorption features (Figure 7, Figure A.6). Table 2 provides the energy ranges and peak width tolerances for fitting each spectral feature. These fitting ranges have been established to provide flexibility in fitting slight differences in peak energies occurring across a range of compositions and oxidation states, while maintaining peak positions that accurately correspond to the specific sulfur features (important for overlapping features such as the $S^{2-}$ and $S^{4+}$ peaks, and the $S^{6+}$ and ionization peaks).

**Table 2.** Peak definitions and fit parameters used for quantification of normalized S-XANES spectra intensities using the XAS Viewer spectral fitting program (Newville, 2013). See **Data supplement** for example peak fit models.

| S-XANES feature | function type / name | peak center bounds (eV) | peak sigma bounds (width) | peak amplitude bounds |
|---|---|---|---|---|
| *overall fit ranges* | | | | |
| peak fit range | - | 2455 – 2550 | - | - |
| pre-edge fit range | - | 2466 – 2487 | - | - |
| *background fitting* | | | | |
| baseline error function | error1 | 2485 (fixed) | 8 (fixed) | 0 – 1.1 |
| baseline Gaussian | gauss1 | 2493 – 2500 | 0 – 10 | 0 – 15 |
| *Sulfur speciation peaks* | | | | |
| sulfide complexes | gauss2 | 2465 – 2470 | 0 – 1 | 0 – ∞ |

| | | | | |
|---|---|---|---|---|
| $S^{2-}$ (sulfide in glass) | gauss3 | 2475.3 – 2477 | 2 – 4 | 0 – ∞ |
| $S^{4+}$ (sulfite) | gauss4 | 2476.8 – 2477.7 | 0.1 – 1 | 0 – ∞ |
| $S^{6+}$ (sulfate) | gauss5 | 2480 – 2482.3 | 0.1 – 3 | 0 – ∞ |
| sulfur ionization peak | gauss6 | 2483.5 – 2486 | 0 – 4 | 0 – ∞ |

To relate the relative fitted peak areas to sulfur speciation, we calibrate our peak fitting method to experimental hydrous basaltic glasses presented in Jugo et al. (2010). Following the same approach as Jugo et al. (2010), we use their completely $S^{2-}$-bearing and completely $S^{6+}$-bearing experimental glasses as reduced and oxidized end-members, and apply linear combination fitting of these end-members to produce representative mixed speciation spectra (Figure A.5). Complete details are provided in the **Supplementary information**.

Jugo et al. (2010) focus their S-XANES calibration on only $S^{2-}$ and $S^{6+}$ peak intensities, and do not include signals from lower energy sulfide-complexes or higher energy features beyond the $S^{6+}$ peak. We follow this approach, and although we fit all spectral features in the calibration glasses, we use only the $S^{2-}$ and $S^{6+}$ peak areas to quantify the sulfur speciation in glasses (Figure 7, Figure A.6). Jugo et al. (2010) describe an exponential function to relate $S^{2-}$ and $S^{6+}$ peak intensities to sulfur speciation, however we find that the following empirical polynomial relationship is more appropriate for our peak fitting method (Figure A.7):

$$S^{6+}/\Sigma S = 0.1733 * (I[S^{6+}]/\Sigma I[S^T])^2 + 0.8343 * (I[S^{6+}]/\Sigma I[S^T]), \text{ [Eq. 1]}$$

where $S^{6+}/\Sigma S$ is the fraction of $S^{6+}$ out of total sulfur in the glass, and $I[S^{6+}]/\Sigma I[S^T]$ is the XANES-measured $S^{6+}$ intensity (Gaussian peak area) out of the combined total intensities of the $S^{6+}$ peak and the broad $S^{2-}$ peak ($I[S^{6+}] + I[S^{2-}] = I[S^T]$). This peak fitting approach accurately reproduces observations from additional glasses synthesized by Jugo et al. (2010) across a range of $fO_2$ and sulfur speciation (Figure A.8). We therefore conclude that our peak fitting approach is similar to the calibration (and this compatible with the thermodynamic relations) originally described by Jugo et al. (2010), while additionally allowing the quantification of a $S^{4+}$ peak. We note that our method is subject to the same limitations as the Jugo et al. (2010) approach, namely, that the linear end-member mixing approach to calibrate mixed sulfur speciation melts is valid. Additional uncertainty arises from inconsistencies with normalizing S-XANES spectra, which can be challenging in sulfur-poor glasses. Unfortunately, raw S-XANES spectra are seldom published, which precludes assessing consistency in normalization approaches between studies. For reproducibility of spectral processing by future workers, it is important that both the

729 raw and the normalized/flattened S-XANES data be made available (see **Data supplement**)
730 (Rose-Koga et al., 2021).

731 The average precision of our S-XANES peak fitting method, based on multiple analyses
732 in single MI and within regions of mid-ocean ridge basalt (MORB) glasses, is ±7% relative (2
733 RSE, 19 analyses in glasses ranging from 0.07 to 0.85 $S^{6+}/\Sigma S$; see **Data supplement**). When
734 considering further uncertainties in the peak fitting calibration and from the non-uniqueness of
735 spectra normalization (particularly in signal-limited samples), we assume the total accuracy of
736 this method to be better than ±10% relative.
737

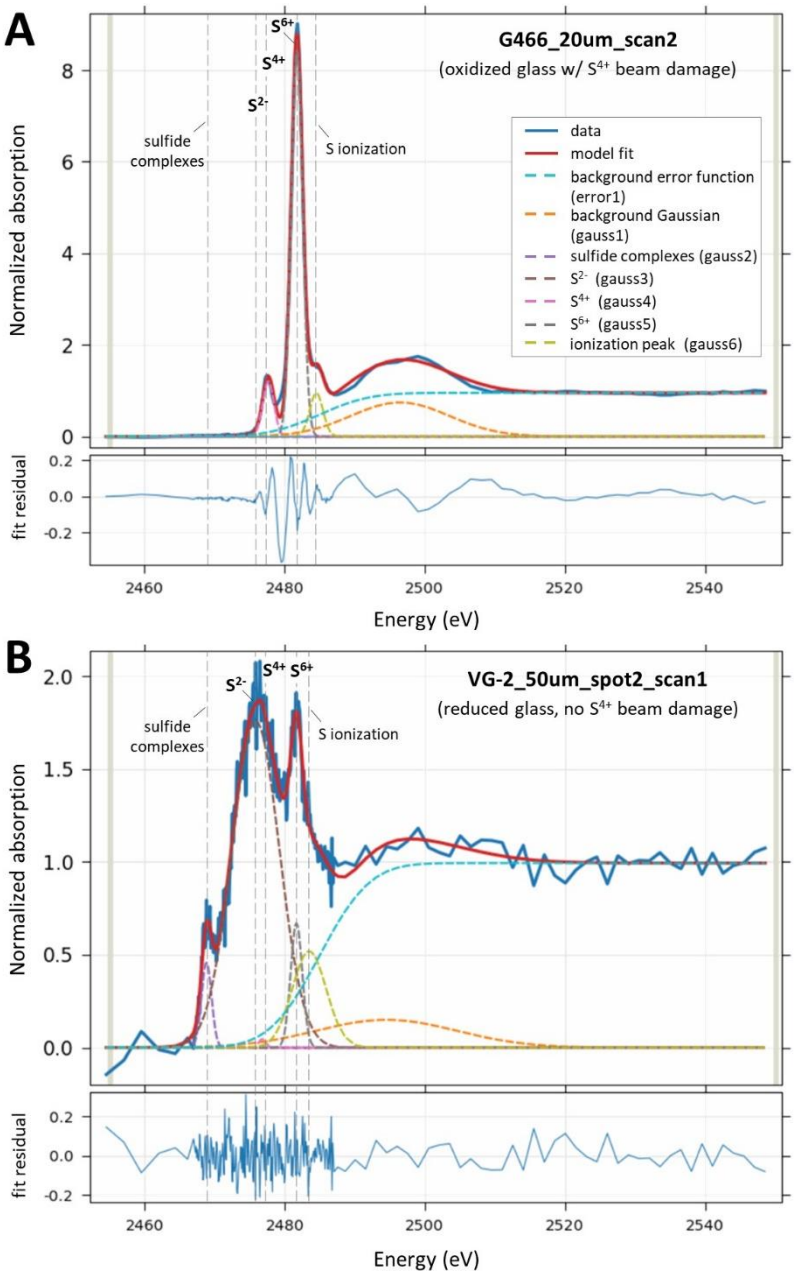


**Figure 7**. *(A)* Example S-XANES peak fitting to oxidized experimental glass G466. This spectrum is the 2nd of 3 repeat scans with a 20×20 μm beam (photon flux density of $1.1\times10^8$ photons/s/μm$^2$) and shows a dominant $S^{6+}$ peak (2480 – 2482.3 eV) and a substantial beam damage-induced $S^{4+}$ peak (2476.8 – 2477.7 eV). No $S^{2-}$ intensity is observed. The fit residual shows slight remaining unfit structure. *(B)* Example S-XANES peak fitting of reduced VG-2 MORB glass analyzed using a 50×50 μm beam (photon flux density of $6.2\times10^6$ photons/s/μm$^2$). The noisier spectrum is due to lower sulfur content in VG-2 than G466, as well as a difference in vertical scale. A main glassy $S^{2-}$ peak (2475.3 – 2477 eV) is present, as well as a lesser $S^{6+}$ peak and a minor sulfide peak (2465 – 2470 eV). Minimal $S^{4+}$ beam damage ingrowth is observed with this diffuse beam analysis (compare to Figure 9). A sulfur-ionization peak (2483.5 – 2486 eV) is present in S-XANES spectra of the both oxidized and reduced glasses. See Table 2 for

identification of peaks and fit parameters. Reference peak position lines may vary slightly between samples depending on bond coordination environments.

### 2.3.3 Correcting S-XANES beam damage

Since we include the $S^{4+}$ peak in our fitting methodology, we can quantitatively separate the beam damage-induced $S^{4+}$ signal from the overlapping broad $S^{2-}$ peak in S-XANES spectra. This was not possible with the Jugo et al. (2010) method because all signal intensity over this region was considered as $S^{2-}$, which would lead to spurious results in beam-damaged spectra (Figures 8, 9). During repeat measurements of hydrous, sulfur-rich, oxidized, anhydrite-saturated experimental basaltic glasses G466 and G479 (50 – 51 wt% $SiO_2$, 9000 – 15000 ppm S, 6.5 – 8.9 wt% $H_2O$, 1300 – 1325 °C, 1.5 – 2.0 GPa; Table 1; Chowdhury and Dasgupta, 2019), we observe that progressive irradiation leads to increasing $S^{4+}$ intensity and concomitant decreasing $S^{6+}$ intensity (Figure 8) (Wilke et al., 2008; Métrich et al., 2009; Konecke et al., 2017). Because these glasses are highly oxidized, they contain no $S^{2-}$ signal to overlap with the $S^{4+}$ peak, which makes observation of the $S^{4+}$ signal straightforward. As expected, increased photon doses with more focused beams cause more rapid $S^{6+}$ to $S^{4+}$ photo-reduction. Comparing the intensity ratio of $S^{4+}$ peak ingrowth and $S^{6+}$ peak loss during progressive beam damage from repeat measurements with photon flux densities ranging from $10^6$ to $10^{10}$ photons/s/μm$^2$, we find that $S^{4+}$ peak ingrowth relates to $S^{6+}$ intensity decrease by a factor of 1.2 ± 0.1 (1 SE; n = 7) (see **Data supplement**). We apply this scaling factor to observed $S^{4+}$ peak intensities in beam damaged samples to restore original $S^{6+}$ peak intensities via:

$$\Sigma I[S^{6+}] = (I[S^{4+}] * F_S^{4+/6+}) + I[S^{6+}], \text{ [Eq. 2]}$$

where $\Sigma I[S^{6+}]$ is the restored total $S^{6+}$ S-XANES intensity, $I[S^{4+}]$ and $I[S^{6+}]$ are the measured Gaussian peak areas from S-XANES intensities, and $F_S^{4+/6+}$ is the $S^{4+}$ to $S^{6+}$ intensity scaling factor (1.2 ± 0.1; though this may be compositionally dependent, as discussed below). The ratio of $S^{6+}$ signal intensity to total sulfur intensity is then:

$$I[S^{6+}] / \Sigma I[S^T] = \Sigma I[S^{6+}] / (I[S^{2-}] + \Sigma I[S^{6+}]), \text{ [Eq. 3]}$$

Inputting this value into our peak fitting calibration based on the Jugo et al. (2010) glass suite (Eq. 1) calculates the beam damage-restored sulfur speciation.

In addition to the obvious $S^{4+}$ peak growth during beam damage of G466 and G479 glasses, we observe the ingrowth of a very small peak between 2471.6 – 2472.0 eV (Figure 8

inset), which is in the energy absorption range attributed to $S^0$ (Fleet et al., 2005; Métrich et al., 2009) or $H_2S$ (Klimm et al., 2012a). This 2471.6 – 2472.0 eV peak is recognized during successive analyses using 2×2, 10×10, and 20×20 μm spots ($10^{10}$ to $10^8$ photons/s/μm$^2$), but is a negligible feature compared to the $S^{4+}$ and $S^{6+}$ signals. We also observe a slight absorption increase in the broad energy range between 2470 – 2475 eV, which overlaps the $S^{2-}$ glassy absorption range. These subtle features are not included in our beam damage correction approach, as peak-fitting such low-intensity features was inconsistent and sensitive to slight variations in the spectra normalization routine. However, these additional features of S-XANES beam damage invite future investigation.

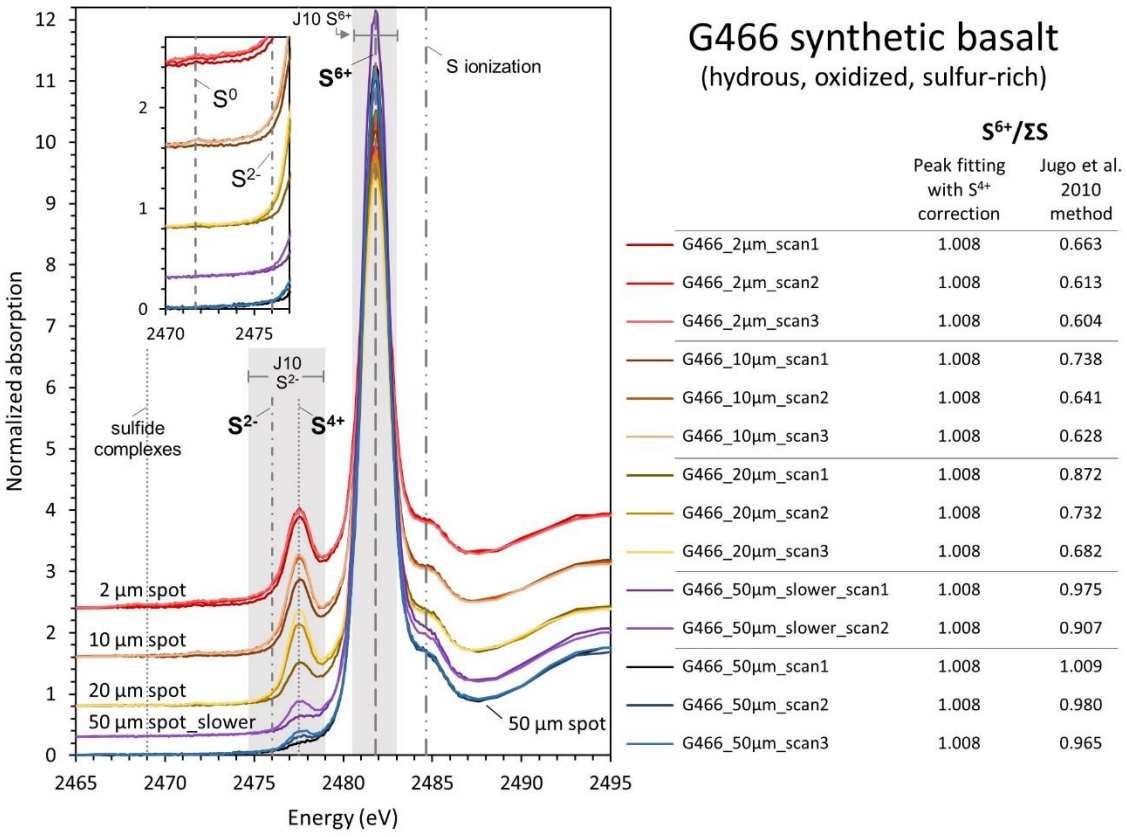


| | $S^{6+}/\Sigma S$ Peak fitting with $S^{4+}$ correction | $S^{6+}/\Sigma S$ Jugo et al. 2010 method |
|---|---|---|
| G466_2μm_scan1 | 1.008 | 0.663 |
| G466_2μm_scan2 | 1.008 | 0.613 |
| G466_2μm_scan3 | 1.008 | 0.604 |
| G466_10μm_scan1 | 1.008 | 0.738 |
| G466_10μm_scan2 | 1.008 | 0.641 |
| G466_10μm_scan3 | 1.008 | 0.628 |
| G466_20μm_scan1 | 1.008 | 0.872 |
| G466_20μm_scan2 | 1.008 | 0.732 |
| G466_20μm_scan3 | 1.008 | 0.682 |
| G466_50μm_slower_scan1 | 1.008 | 0.975 |
| G466_50μm_slower_scan2 | 1.008 | 0.907 |
| G466_50μm_scan1 | 1.008 | 1.009 |
| G466_50μm_scan2 | 1.008 | 0.980 |
| G466_50μm_scan3 | 1.008 | 0.965 |

**Figure 8**. Normalized spectra of oxidized, anhydrite-saturated, experimental glass G466 with repeat measurements in different locations with progressively greater photon flux densities ($6.2\times10^6$, $4.3\times10^6$, $1.1\times10^8$, $4.2\times10^8$, and $1.1\times10^{10}$ photons/s/μm$^2$ for the 50μm, 50μm_slower, 20μm, 10μm, and 2μm scans, respectively). Spectra have been vertically shifted for clarity. The ingrowth of $S^{4+}$ (2476.8 – 2477.7 eV) at the expense of $S^{6+}$ (2480 – 2482.3 eV) is seen in repeat measurements at all spot sizes, and is increasingly pronounced with more focused beams. $S^{4+}$ ingrowth stops after reaching a maximum intensity during the first focused 2×2 μm spot analysis,

with no further ingrowth during subsequent analyses. *(inset)* Detailed view of the 2470 – 2476 eV region showing the ingrowth of a small peak at ~2471.7 eV and a slight absorption increase across 2470 – 2475 eV in analyses with focused beams. Each individual scan length was 5 minutes, except for G466_50um_scans that were each 10 minutes. $S^{6+}/\Sigma S$ calculations using the peak fitting approach and correcting for $S^{4+}$ photo-reduction are compared with $S^{6+}/\Sigma S$ calculated using the Jugo et al. (2010) method ("J10" gray $S^{2-}$ and $S^{6+}$ regions [energy shifted as discussed]), where the $S^{4+}$ photo-reduction peak would be counted as part of the $S^{2-}$ signal. Reference peak position lines may vary slightly between samples.

### 2.3.4 Observations of natural glasses and melt inclusions

We observe the same rapid $S^{6+}$ to $S^{4+}$ photo-reduction in numerous natural glasses. Hydrous basaltic MI from the southern Cascades (up to 3.7 wt% $H_2O$) undergo rapid photo-reduction (Muth and Wallace, 2021), which is consistent with hydrous basalts being highly susceptible to speciation changes during X-ray irradiation (Cottrell et al., 2018; Moussallam et al., 2019). However, we also observe rapid photo-reduction during S-XANES analyses of low-$H_2O$ tholeiitic basaltic glasses that have been observed to be very stable during Fe-XANES analyses (Cottrell et al., 2009; Zhang et al., 2018). Repeated rapid S-XANES scans of the MORB glass standard VG-2 (NMNH 111240-52; Juan de Fuca ridge) again show a marked decrease in $S^{6+}$ and ingrowth of $S^{4+}$ during successive analyses (Figure 9). S-XANES measurements of VG-2 have been presented elsewhere (e.g., Head et al., 2018), but have typically been analyzed with a more focused beam and longer measurement times than used here, which we observe to cause a near complete conversion of $S^{6+}$ to $S^{4+}$. VG-2 glass is relatively reduced (0.15 $Fe^{3+}/\Sigma Fe$, fayalite-magnetite-quartz buffer [FMQ] +0.0; Zhang et al., 2018) so that the original $S^{6+}$ is low and the photo-reduction $S^{4+}$ peak is correspondingly small. The small $S^{4+}$ peak is therefore difficult to discern from the dominant $S^{2-}$ peak, which potentially explains why beam damage in VG-2 glass has not been previously recognized. A North Pacific MORB glass analyzed via S-XANES with a defocused beam by Métrich et al. (2009) also had a recognizable small $S^{6+}$ peak, consistent with our observations of VG-2. Applying our peak fitting and $S^{4+}$ to $S^{6+}$ correction approach to the least beam-damaged VG-2 analyses (50×50 μm spot size; $1.1\times10^7$ photons/s/$\mu m^2$ flux density), we estimate that VG-2 MORB glass has 0.079 ± 0.003 $S^{6+}/\Sigma S$ (1 SE, n = 4). S-XANES measurements of two additional MORB glasses, JDF-46N and ALV892-1 (Woods Hole Oceanographic Institution, Northeast National Ion Microprobe Facility internal standards), at low photon flux densities ($2 – 3\times10^7$ photons/s/$\mu m^2$) give similar $S^{6+}/\Sigma S$ of 0.081 ± 0.001 and 0.093

± 0.001, respectively (1 SE, n=4 for each glass). Tests at higher photon flux densities ($10^8$ – $10^{10}$ photons/s/μm$^2$) or with long analysis durations (>6 minutes) show that JDF-46N and ALV892-1 also undergo rapid $S^{6+}$ to $S^{4+}$ photo-reduction (Figure 10), indicating a common susceptibility for X-ray induced photo-reduction among low-$H_2O$ MORB samples.

The measured 0.08 – 0.09 $S^{6+}/\Sigma S$ in these three MORB samples are similar to the upper end of the 0.03 – 0.07 $S^{6+}/\Sigma S$ range measured in MORB glasses via EPMA S-*K*α wavelength shift (Wallace and Carmichael, 1994) (although the EPMA-measured samples may have suffered from electron beam-induced photo-oxidation [Jugo et al., 2010]). These measurements are all elevated compared to the 0.00 – 0.02 $S^{6+}/\Sigma S$ measured by S-XANES in four MORB glass samples by Jugo et al. (2010). Based on global MORB average $fO_2$ estimates of FMQ -0.17 ± 0.15 (0.014 ± 0.01 $Fe^{3+}/\Sigma Fe$) by Cottrell et al. (2020) or FMQ +0.1 by Berry et al. (2018), the Jugo et al. (2010) relationship of $S^{6+}$ to $fO_2$ predicts that MORB glasses should contain almost exclusively sulfide (≤0.01 $S^{6+}/\Sigma S$). However, our observations indicate that MORB glasses are not universally sulfate-free and, at least in the three localities analyzed here, contain low but resolvable $S^{6+}$ (up to 0.09 $S^{6+}/\Sigma S$).

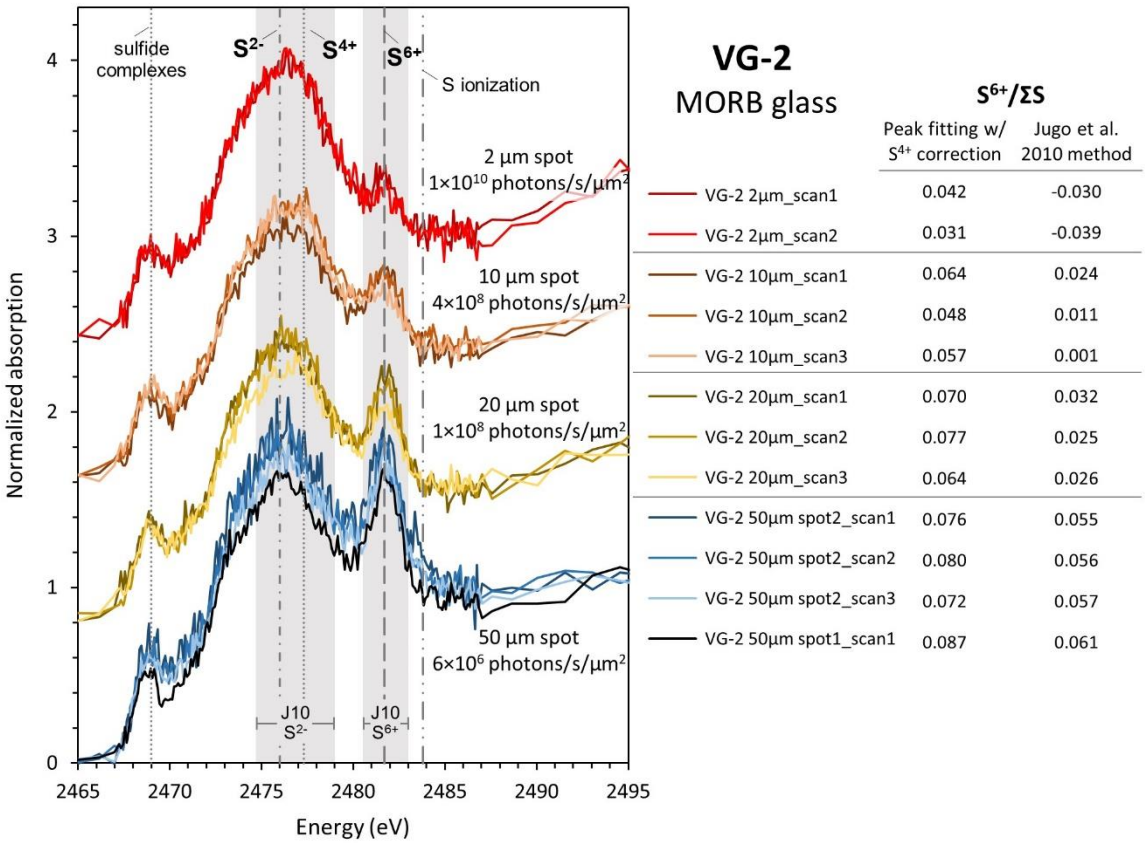


**VG-2**
MORB glass

| | $S^{6+}/\Sigma S$ Peak fitting w/ $S^{4+}$ correction | $S^{6+}/\Sigma S$ Jugo et al. 2010 method |
|---|---|---|
| VG-2 2µm_scan1 | 0.042 | -0.030 |
| VG-2 2µm_scan2 | 0.031 | -0.039 |
| VG-2 10µm_scan1 | 0.064 | 0.024 |
| VG-2 10µm_scan2 | 0.048 | 0.011 |
| VG-2 10µm_scan3 | 0.057 | 0.001 |
| VG-2 20µm_scan1 | 0.070 | 0.032 |
| VG-2 20µm_scan2 | 0.077 | 0.025 |
| VG-2 20µm_scan3 | 0.064 | 0.026 |
| VG-2 50µm spot2_scan1 | 0.076 | 0.055 |
| VG-2 50µm spot2_scan2 | 0.080 | 0.056 |
| VG-2 50µm spot2_scan3 | 0.072 | 0.057 |
| VG-2 50µm spot1_scan1 | 0.087 | 0.061 |

**Figure 9**. Normalized S-XANES spectra of MORB glass standard VG-2 with repeat measurements in different locations using progressively greater photon flux densities ($6.4\times10^6$, $1.1\times10^8$, $4.3\times10^8$, $1.1\times10^{10}$ photons/s/µm$^2$ for the 50µm, 20µm, 10µm, and 2µm scans, respectively). Spectra have been vertically shifted for clarity. The ingrowth of $S^{4+}$ (2476 – 2477.7 eV) and loss of $S^{6+}$ (2480.5 – 2483.3 eV) is increasingly apparent during analysis with more focused beams. Measurements with a fully focused 2×2 µm beam cause the $S^{6+}$ signal to be almost completely lost. Note the difficulty of recognizing the $S^{4+}$ peak against the dominant $S^{2-}$ broad peak at 2472 – 2480 eV, giving the illusion of a beam damage-free spectra. Each individual scan duration was 5 minutes. $S^{6+}/\Sigma S$ calculations using the peak fitting approach and correcting for $S^{4+}$ photo-reduction are compared with $S^{6+}/\Sigma S$ calculated using the Jugo et al. (2010) method ("J10" gray $S^{2-}$ and $S^{6+}$ regions [energy shifted as discussed]), where the $S^{4+}$ photo-reduction peak would be counted as part of the $S^{2-}$ signal. Reference peak position lines may vary slightly between samples.

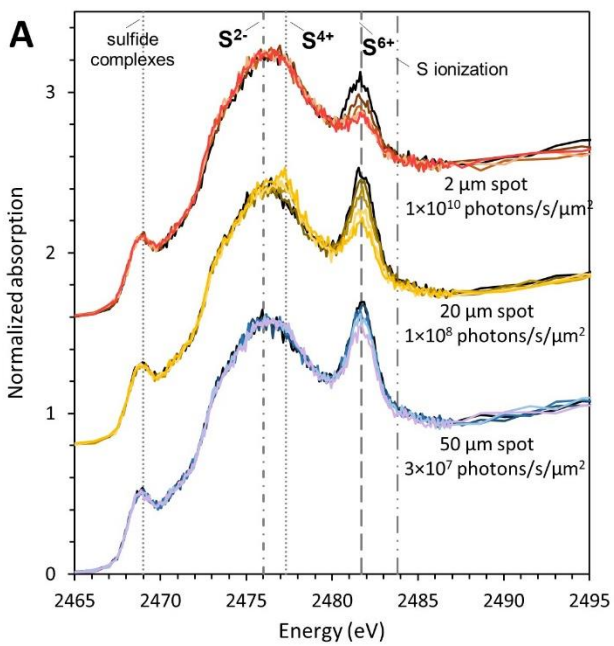


| JDF-46N MORB glass | Total analysis time (s) | $S^{6+}/\Sigma S$ Peak fitting with $S^{4+}$ correction | $S^{6+}/\Sigma S$ Peak fitting w/ no $S^{4+}$ correction |
|---|---|---|---|
| JDF-46N 2µm_scan1 | 304 | 0.062 | 0.055 |
| JDF-46N 2µm_scan2 | 622 | 0.052 | 0.043 |
| JDF-46N 2µm_scan5 | 1575 | 0.035 | 0.034 |
| JDF-46N 2µm_scan10 | 3168 | 0.037 | 0.036 |
| JDF-46N 2µm_scan20 | 6351 | 0.044 | 0.041 |
| JDF-46N 20µm_scan1 | 304 | 0.082 | 0.082 |
| JDF-46N 20µm_scan2 | 622 | 0.077 | 0.075 |
| JDF-46N 20µm_scan5 | 1575 | 0.069 | 0.064 |
| JDF-46N 20µm_scan10 | 3168 | 0.061 | 0.051 |
| JDF-46N 20µm_scan20 | 6351 | 0.053 | 0.039 |
| JDF-46N 50µm_scan1 | 304 | 0.084 | 0.084 |
| JDF-46N 50µm_scan2 | 622 | 0.077 | 0.077 |
| JDF-46N 50µm_scan5 | 1575 | 0.080 | 0.078 |
| JDF-46N 50µm_scan10 | 3168 | 0.071 | 0.070 |
| JDF-46N 50µm_scan20 | 6351 | 0.072 | 0.068 |

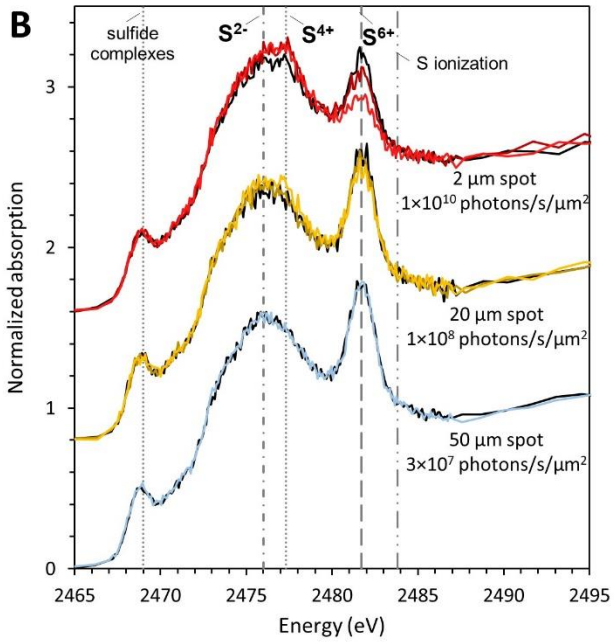


| ALV892-1 MORB glass | Total analysis time (s) | $S^{6+}/\Sigma S$ Peak fitting with $S^{4+}$ correction | $S^{6+}/\Sigma S$ Peak fitting w/ no $S^{4+}$ correction |
|---|---|---|---|
| ALV892-1 2µm_scan1 | 152 | 0.071 | 0.068 |
| ALV892-1 2µm_scan2 | 319 | 0.062 | 0.054 |
| ALV892-1 2µm_scan6 | 986 | 0.048 | 0.042 |
| ALV892-1 20µm_scan1 | 152 | 0.090 | 0.089 |
| ALV892-1 20µm_scan2 | 319 | 0.088 | 0.088 |
| ALV892-1 20µm_scan6 | 986 | 0.081 | 0.079 |
| ALV892-1 50µm_scan1 | 304 | 0.097 | 0.097 |
| ALV892-1 50µm_scan2 | 622 | 0.092 | 0.092 |

**Figure 10**. Normalized S-XANES spectra of MORB glasses JDF-46N and ALV892-1 with repeat measurements in different locations using progressively greater photon flux densities. Spectra have been vertically shifted for clarity. Spectra shown are examples from long sequences of repeated analyses (20 repeated scans for JDF-46N; 2 – 6 repeated scans for ALV892-1). Cumulative irradiation durations are listed on the right, and $S^{6+}/\Sigma S$ calculations using the peak fitting approach with and without correcting for $S^{4+}$ photo-reduction are compared. As in Figure 9, the ingrowth of $S^{4+}$ (2476 – 2477.7 eV) and loss of $S^{6+}$ (2480.5 – 2483.3 eV) is increasingly apparent during longer analyses and those with more focused beams. Note that $S^{4+}$ corrections do not reproduce the $S^{6+}/\Sigma S$ observed with low photon density measurements, indicating that

challenge of applying beam damage corrections in reduced glasses with overlapping $S^{2-}$ and $S^{4+}$ peak areas. Reference peak position lines may vary slightly between samples.

We also observe $S^{6+}$ to $S^{4+}$ photo-reduction during S-XANES analyses of low-$H_2O$ basaltic MI samples from the 2018 lower East Rift Zone (LERZ) fissure eruption of Kīlauea Volcano, HI (≤0.3 wt% $H_2O$ [Lerner et al., 2021]). Depending on the degree of atmospheric interaction prior to quenching, the Kīlauea olivine-hosted MI range from reduced to highly oxidized (FMQ -0.7 to +2.4; Lerner, 2020). S-XANES beam damage occurs in Kīlauea MI throughout this wide range of oxidation states (Figure 11). The $S^{6+}$ to $S^{4+}$ photo-reduction during X-ray irradiation in Kīlauea MI and in MORB glasses is particularly interesting because these low-$H_2O$ ocean island basalt (OIB) and MORB glasses are stable during Fe-XANES measurements (Figure 11), having Φ values ≤0.1 (Table 1). These observations highlight that major (e.g., iron) and minor (e.g., sulfur) elements may have different susceptibilities to X-ray induced beam damage (Gonçalves Ferreira et al., 2013). Alternatively or additionally, the different responses of iron and sulfur during irradiation may be related to their behavior as non-volatile and volatile elements, or to the ratio of redox couples (e.g., S/Fe concentration ratios) (Hughes et al., 2020).

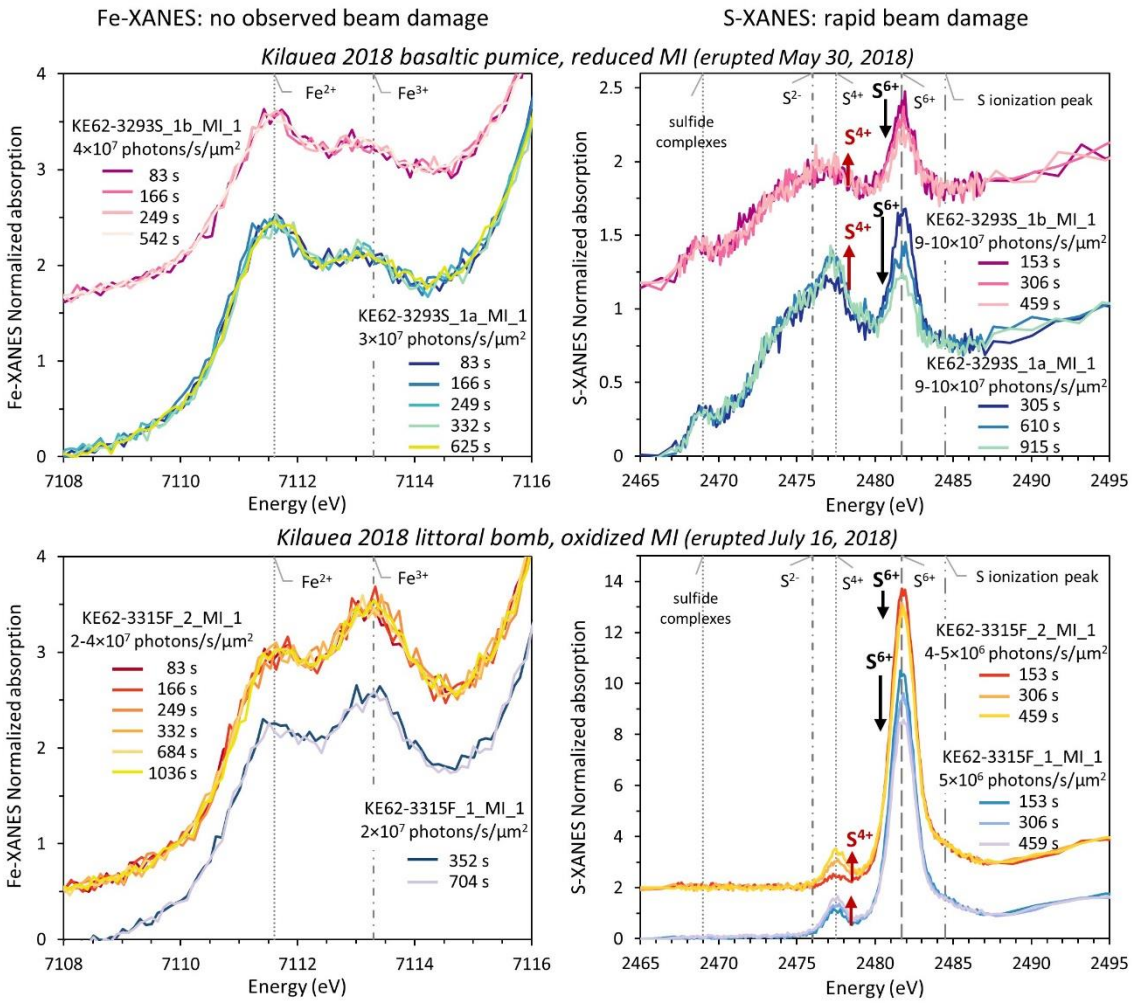


**Figure 11**. Four MI from the Kīlauea 2018 LERZ eruption were analyzed by both Fe- and S-XANES and exhibit differing susceptibilities to beam damage. Fe-XANES *(left)* and S-XANES *(right)* analyses were conducted in different locations within the same MI. Repeated rapid analyses were conducted for each technique, as described in the text, and the cumulative ending time in seconds (s) for successive scans are shown. Melt inclusions in both reduced, rapidly quenched basaltic pumice (KE62-3293S, *top*) and oxidized littoral bomb samples (KE62-3315F, *bottom*) exhibit no $Fe^{2+}$ to $Fe^{3+}$ photo-oxidation during repeat measurements, but the same MI undergo rapid $S^{6+}$ to $S^{4+}$ photo-reduction during S-XANES analyses. All MI contain ≤0.3 wt% $H_2O$ and have $\Phi$ <0.1. Spot sizes were 10×10 um for Fe-XANES and 10×10 or 20×20 um for S-XANES resulting in photon flux densities of 2 – 4×$10^7$ and 4 – 10×$10^7$ photons/s/µm$^2$ for Fe- and S-XANES measurements, respectively. Vertical lines are approximate reference peak positions, which may vary slightly between samples.

### 2.3.5 Discussion and summary

The S-XANES peak fitting calibration and the determination of the $S^{4+}$ to $S^{6+}$ intensity scaling factor could be improved with calibrations that include different compositions beyond the

basalts tested here (experimental glasses of Jugo et al. [2010] and Chowdhury and Dasgupta [2019]). In particular, the concentration of Ca and $Fe^{2+}$ may exert some control on sulfur speciation at given $fO_2$ conditions and potentially on beam damage susceptibility in glasses (Graz et al., 2007; Klimm et al., 2012a,b). $H_2O$-content may also play a role in S-XANES beam damage susceptibility (Wilke et al., 2008) as it does in Fe-XANES photo-oxidation (Cottrell et al., 2018). As an example, calculations of sulfur speciation in MORB glasses using the $S^{4+}$ to $S^{6+}$ scaling factor of 1.2 to account for sulfur photo-reduction result in systematically lower $S^{6+}/\Sigma S$ for progressively more beam damaged analyses (from 0.09 to 0.03 $S^{6+}/\Sigma S$) (Figures 9, 10). This indicates that the $S^{4+}$ to $S^{6+}$ scaling factor is likely larger for anhydrous, reduced basalt than what we have determined for hydrous, oxidized basaltic glass. A $S^{4+}$ to $S^{6+}$ scaling factor of >3 is required to equate the $S^{6+}/\Sigma S$ of highly beam damaged MORB analyses with the undamaged measurements made using very low photon flux densities. However, we note that fitting the $S^{4+}$ peak is challenging in more reduced samples due to the overlap of the dominant $S^{2-}$ peak with the relatively minor $S^{4+}$ peak, and we might be under-fitting the $S^{4+}$ peak in the MORB spectra. Additionally, in samples with mixed sulfur speciation, the slight beam damage-induced energy increase in the 2470 – 2475 eV range (Figure 8 inset) would be completely masked by, and included within, the broad $S^{2-}$ peak area. Further characterizing the complete range of sulfur complexing and valence changes during beam damage will be important for further improving S-XANES correction methods. The uncertainties in the $S^{4+}$ to $S^{6+}$ intensity corrections underscore that the foremost approach during S-XANES measurements should be to minimize beam damage as much as possible, so that the overall uncertainties stemming from any $S^{4+}$ corrections are small.

In summary, S-XANES beam damage can occur in both hydrous and anhydrous silicate glasses, but can be identified through repeat rapid scans by the presence and growth of a $S^{4+}$ peak. If beam damage is found to occur, we suggest focusing on the least damaged spectra for each measurement, and then applying a $S^{4+}$ to $S^{6+}$ scaling factor to restore $S^{4+}$ signal to the original $S^{6+}$ intensity. In high-sulfur samples, where signal intensity is sufficient even with rapid scans, this is the ideal approach as beam damage is first limited and then restored to a good approximation of original $S^{6+}$ intensity. Low-sulfur samples may require merging multiple rapid scans to obtain quantifiable spectra, despite the longer cumulative analysis time inducing more photo-reduction. In long duration or merged scans, irradiation-induced $S^{4+}$ signal can still be

restored to $S^{6+}$ intensity, and although this introduces greater uncertainty (due to imprecisely known $S^{4+}$ to $S^{6+}$ scaling factors), it is still a better approach than not applying any beam damage correction. In highly oxidized samples lacking $S^{2-}$, accounting for $S^{4+}$ is less important as it can simply be assumed that all sulfur was originally present as $S^{6+}$. However, in samples with mixed sulfur speciation, separating any $S^{4+}$ photo-reduction signal from the overlapping $S^{2-}$ peak, and restoring the $S^{4+}$ to original $S^{6+}$ is important in accurately determining the initial sulfur speciation of the glass.

### 3.1 Identifying Fe-oxide nanolite crystals in Fe-XANES spectra

In addition to beam damage concerns during XANES analyses of glasses, the possible cryptic occurrence of nanolite crystals in glasses must also be considered to avoid spurious interpretations of XANES spectra. Nanolites are minerals in the sub-micron range that are typically undecipherable with optical microscopes or even with electron microscopes, but can form in MI during quenching under certain conditions. In some settings, dispersed nanolite crystals become large enough to appear as a fine "dust" within MI (Danyushevsky et al., 2002; Wallace et al., 2003). It has been suggested that Fe-oxides and sulfides may form in MI during cooling and/or diffusive $H_2O$-loss (Danyushevsky et al., 2002; Rowe et al., 2007; Di Genova et al., 2017, 2018; 2020; Head et al., 2018). Di Genova et al. (2017, 2018) observe that Fe-oxide (magnetite) nanolites preferentially occur in $H_2O$-rich glasses (≥2.5 wt% $H_2O$) across a range of compositions, suggesting that high $H_2O$ promotes nanolite formation during quenching. This might occur, for example, because increased $H_2O$ lowers the glass transition temperature, resulting in a larger cooling interval in the liquid state for $H_2O$-rich melts (Deubener et al., 2003). The presence of nanolites complicates XANES, Raman, and EPMA redox measurements in glasses because the bonding coordination in nanolite minerals may lead to different relationships between ion abundances and signal intensities compared to calibrated relationships in glasses.

Fortunately, the short-range ordering of iron and sulfur in mineral phases can be readily detected via XANES and Raman spectral techniques (Wilke et al., 2006; Di Genova et al., 2017, 2018; 2020; Head et al., 2018). Magnetite nanolites have been spectrally identified by Raman measurements in MI from basalts, dacites, and trachytes containing >4.5 wt% $FeO^T$ and ≥2.5

970 wt% $H_2O$ (Di Genova et al., 2017, 2018). Magnetite nanolite abundance correlates with more
971 oxidized (EPMA-calculated) redox states of MI (Hughes et al., 2018), although it is unclear if
972 nanolites actually form in more oxidized MI, or rather that the presence of nanolites affects the
973 redox quantification. Ni-, V-, and S-XANES have been used by Farges et al. (2001) to identify
974 Ni-bearing nanolites in hydrous albitic experimental glasses (≥ 4.5 wt% $H_2O$) and by Head et al.
975 (2018) to identify V- and S-bearing spinel and sulfide nanolites in natural basaltic MI from
976 Nyamuragira volcano (D.R. Congo). Finally, Fe-XANES has been used by Wilke et al. (2006) to
977 identify the formation of Fe-oxide nanolites during the slow quenching of hydrous haplogranitic
978 experimental glasses (where 0.06 – 1.5 μm diameter maghemite nanolites were confirmed by
979 TEM).
980 Here, we build on the observations of Wilke et al. (2006) and show that Fe-XANES
981 measurements can identify the cryptic occurrence of Fe-oxide nanolites in naturally quenched,
982 optically glassy MI. We conducted Fe-XANES measurements of doubly-intersected dacitic-
983 rhyolitic MI from the 2006 eruption of Augustine Volcano (AK, USA) (Lerner, 2020) and of
984 basaltic MI from Cerro Negro (Nicaragua) (Gaetani et al., 2012). A number of these MI contain
985 a sharp absorption peak at ~7129.5 eV that is similar to the absorption edge feature observed in
986 magnetite phenocrysts from both Augustine and oxidized Kīlauea 2018 LERZ samples (Figure
987 12). This magnetite-like peak indicates increased crystalline ordering of iron in the glasses due to
988 Fe-oxide nanolites (Wilke et al., 2006). A magnetite-like peak was also observed in Fe-XANES
989 measurements of optically glassy quartz-hosted MI from Central Andean volcanic centers by
990 Grocke et al. (2016), who similarly considered this feature to indicate Fe-oxide nanolite
991 interference.
992 Melt inclusions in Augustine feldspar and pyroxene grains that contain Fe-oxide
993 (presumably magnetite or maghemite) nanolites are consistently a brown color, although no
994 distinct fine-scale crystals are observable with either optical or electron microscopes (Figures 12,
995 13). Optically colorless MI are also present in the same samples from Augustine, and these
996 colorless MI have smooth Fe-XANES absorption edge spectra that are indicative of glass with no
997 magnetite-like structure (Figures 12, 13). The occurrence of colorless and brown MI, even within
998 the same sample, has been long recognized, and the cause and importance of MI glass color has
999 been much debated. Although some studies have found that colorless MI contain lower $H_2O$ and
1000 higher $CO_2$ than co-occurring brown MI, other studies find negligible differences in volatiles or

major element compositions between different colored MI (Wallace et al., 1999; Myers et al., 2016; Myers, 2017). However, Fe-XANES analyses show that the color of Augustine MI consistently reflects the presence or absence of magnetite nanolites. These findings are consistent with observations of Fe-oxide (and other crystalline phases) nanolites causing the dark color of natural obsidian and rhyolitic glass (e.g., Sharp et al., 1996; Castro et al., 2005; Ma et al., 2007; Tuffen et al., 2021; Galoisy and Calas, 2021). Iron nanolite-bearing Augustine MI have highly variable calculated $Fe^{3+}/\Sigma Fe$, but in general, these MI are more $Fe^{3+}$-rich compared to colorless, nanolite-free MI from the same tephra sample (Lerner, 2020). However, it is again unclear whether this observation reflects an increased oxidation state within the nanolite-bearing MI or if it is a consequence of greater $Fe^{3+}$ signal from the crystalline nanolite phases. Importantly, the presence of Fe-oxide nanolites may invalidate the Fe-XANES centroid energy to $Fe^{3+}/\Sigma Fe$ calibrations for glasses. Until further research is undertaken to investigate such effects on XANES calibrations, spectra containing nanolite signatures should be interpreted cautiously. To help focus sample selection and avoid nanolite-induced complications during synchrotron analyses, Raman spectra could be acquired prior to XANES analyses to identify whether nanolites are present in target glasses (Di Genova et al., 2017, 2018).

We note that many brown-colored MI in more basaltic compositions have clean glassy XANES spectra with no evidence of nanolites (e.g., many Kīlauea LERZ and southern Cascades olivine-hosted MI studied here), so MI color alone does not always indicate the presence of Fe-oxide nanolites. Future efforts to characterize compositional, temperature, and $H_2O$ variations between co-occurring brown and colorless MI in the same units will better clarify the processes that govern Fe-oxide nanolite formation and MI glass color.

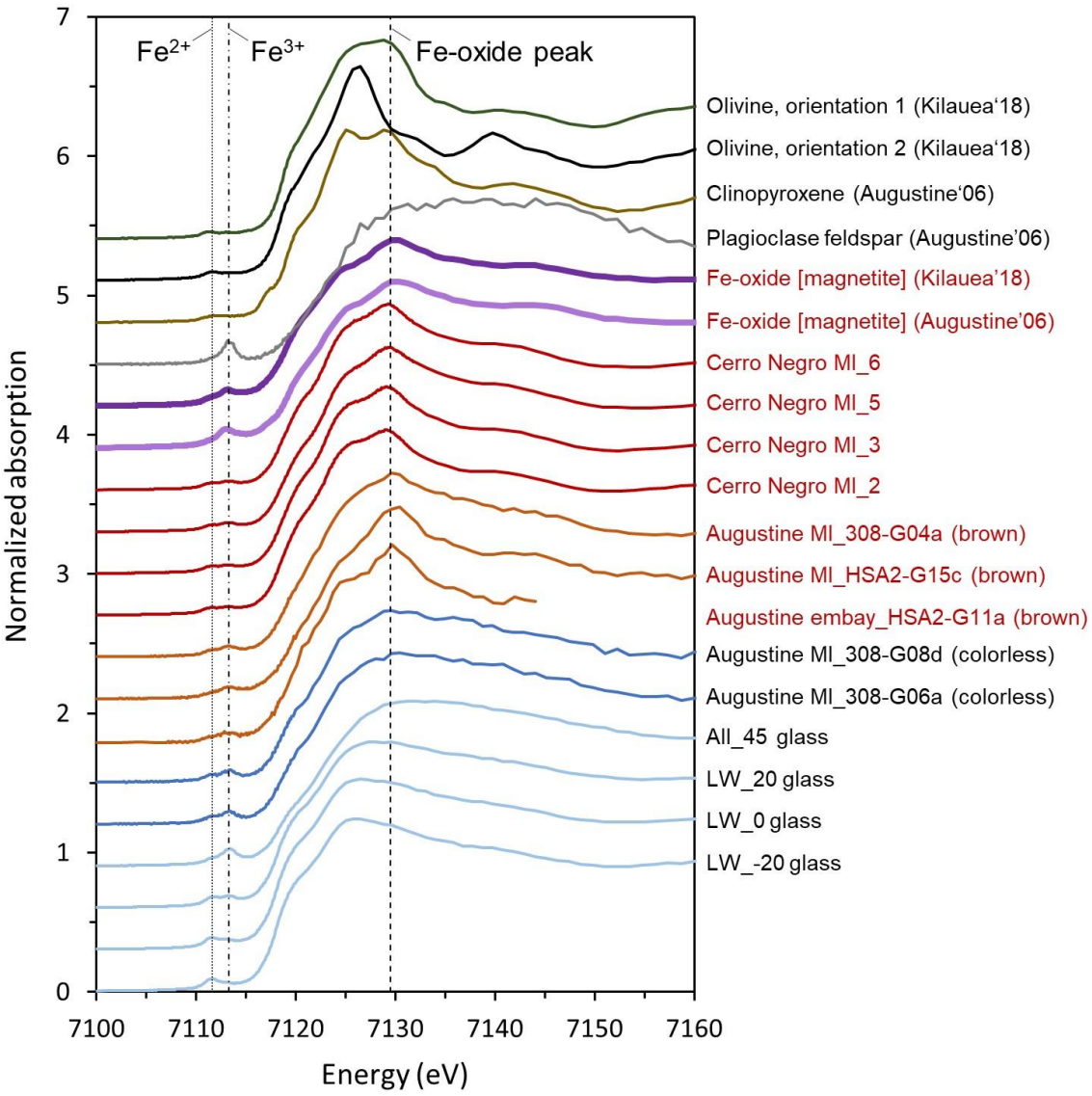


**Figure 12**. Normalized Fe-XANES spectra of mineral spectra (olivine, clinopyroxene, feldspar, magnetite), reference glasses (LW series, AII_45; Cottrell et al., 2009), and doubly-intersected MI or melt embayment glasses from Augustine 2006 (samples shown in Figure 13) and Cerro Negro (see **Data supplement**). Brown-colored dacitic-rhyolitic glasses from Augustine (orange lines) have a prominent peak at ~7129.5 eV that closely resemble magnetite spectra (thick purple lines), indicating the presence of Fe-oxide nanolites. Cerro Negro olivine-hosted basaltic MI (red lines) also have a 7129.5 eV signature of magnetite nanolites. Colorless MI from Augustine (blue lines) have glassy spectra, similar to oxidized reference glasses LW_20 and AII_45 (FMQ +2 and +4.5, respectively). Spectra have been vertically shifted for clarity. The lines labeled $Fe^{2+}$ and $Fe^{3+}$ refer to the approximate peak positions of the first and second pre-edge doublet.

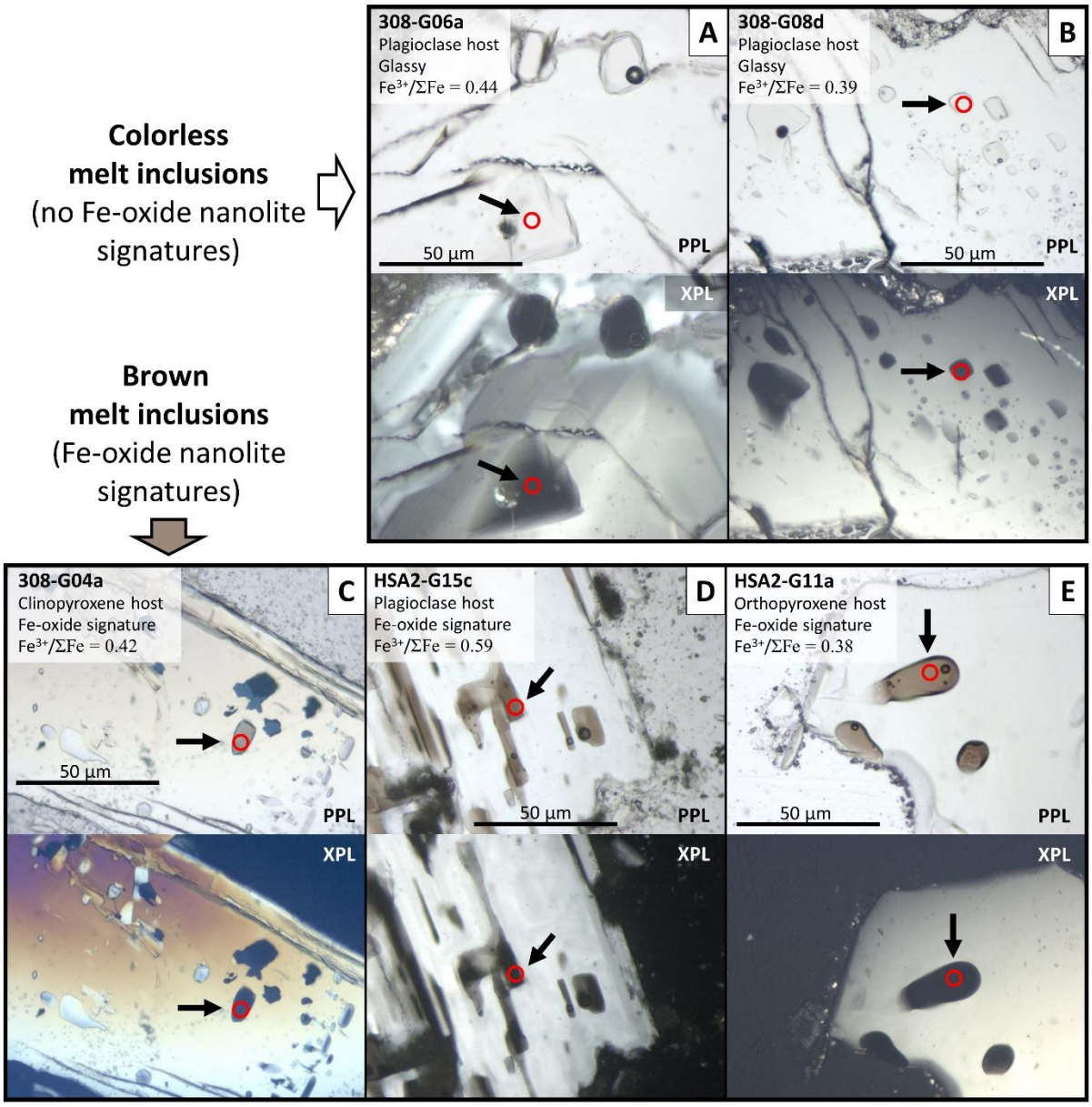


**Figure 13**. Doubly-intersected dacitic-rhyolitic MI (A, B, C, D) and melt embayments (E) erupted from Augustine in 2006. *(top)* Colorless glasses (A, B) and *(bottom)* brown glasses with Fe-oxide nanolite spectral signatures (C, D, E) are present in inclusions and embayments within plagioclase (A, B, D, E) and pyroxene (C). Each two-pane panel shows images with plane polarized light (PPL) and through crossed polarizers (XPL), with full glass extinction in XPL showing where MI are doubly-intersected for host-free Fe-XANES analysis. All Fe-XANES analyses were conducted with a 5×5 µm spot size (~$1.4\times10^8$ photons/s/µm$^2$ flux densities), and spectra are shown in Figure 12. Photo-oxidation was not observed during repeated analyses in these glasses. $Fe^{3+}/\Sigma Fe$ was calculated from the felsic glass calibration of Fiege et al. (2017), although we note that the presence of Fe-oxide nanolites in the brown MI may invalidate such $Fe^{3+}/\Sigma Fe$ calculations.

### 4.1 Conclusions and implications

Accurate XANES measurements are essential for inferring magma redox state from iron and sulfur valence states in quenched glasses. Using repeated, rapid Fe- and S-XANES measurements and implementing a new peak-fitting calibration for S-XANES, we have developed time-dependent corrections to identify and correct for beam damage during Fe- and S-XANES analyses of silicate glasses. Beam damage corrections for iron photo-oxidation and sulfur photo-reduction are determined for each individual analysis rather than applying generalized corrections. This allows versatility to account for composition differences and the effects of variable $H_2O$ concentrations in MI that are commonly found in an individual tephra sample, which can influence beam damage susceptibility. Testing these beam damage correction methods on hydrous experimental basalts, we show that Fe- and S-XANES measurements can be reliably made even on beam-sensitive glasses. Additional studies of the mechanisms and compositional dependence of S-XANES beam damage could further improve the photo-reduction correction method that we have introduced here. Additionally, using Fe-XANES, we demonstrate the occurrence of cryptic Fe-oxide nanolites in naturally quenched MI. Melt inclusions containing nanolite phases may invalidate Fe- and S-XANES calibrations for elemental valence and speciation in glasses, and such spectra should be interpreted with caution.

The analytical techniques presented here extend the ability to reliably measure iron valence and sulfur speciation in small and/or hydrous MI, which can undergo substantial beam damage during XANES analyses. These methods will allow further exploration of the redox behavior in hydrous systems, such as magmatic arcs and high-$H_2O$ intraplate volcanic settings. Measurements of redox conditions in magmatic arc glasses are of particular interest to assess whether subduction inputs oxidize the sub-arc mantle and the relative importance of $fO_2$ in controlling volcanic degassing and the formation of porphyry copper ore deposits.

We demonstrate that irradiation-induced changes in S-XANES spectra occur rapidly even in $H_2O$-poor MORB and OIB glasses that do not experience beam damage during Fe-XANES analysis. This raises the possibility that other multivalent trace element may similarly be subject to variation during X-ray analysis, even in relatively anhydrous glasses. The time-dependent analytical techniques presented here can be extended to XANES analyses of other multivalent

trace elements, which are being increasingly applied to volcanic glasses (e.g., V-, Cr-, Cu-XANES; Sutton et al., 2020), to assess whether changes in valence or molecular complexing may be occurring during irradiation. Additional research into the mechanisms underlying nanolite formation and irradiation-induced beam damage will continue to improve our understanding of these phenomena and how they can be better accounted for.

## Acknowledgements

This manuscript was significantly improved thanks to constructive input from journal reviewers and editors. We thank D. Johnston and J. Watkins (University of Oregon), the U.S. Geological Survey's Hawaiian Volcano Observatory, and the Smithsonian Institution's Department of Mineral Sciences for access to some of the samples analyzed in this study. We also thank J. Donovan and J. Chouinard (University of Oregon) for EPMA assistance. This research used resources of the Advanced Photon Source, a U.S. Department of Energy (DOE) Office of Science User Facility operated for the DOE Office of Science by Argonne National Laboratory under Contract No. DE-AC02-06CH11357. We acknowledge the support of GeoSoilEnviroCARS at the Advanced Photon Source, which is supported by NSF - Earth Sciences (EAR-1128799), and the Department of Energy, Geosciences (DE-FG02-94ER14466). A.H.L and M.J.M. acknowledge support from the National Science Foundation Graduate Research Fellowship Program (NSF-GRFP) under grant 1309047 and internships provided through the Graduate Research Internship Program (GRIP). P.J.W. acknowledges funding support from the National Science Foundation under grant EAR-1834959. Any findings and conclusions or recommendations expressed in this material are those of the authors and do not necessarily reflect the views of the National Science Foundation.

## Author Contributions

A.H.L. and M.J.M. conceived of the project and led sample preparation, analysis, data synthesis, and authoring. P.J.W., A.L., and M.N. aiding in project design, data interpretation, and manuscript editing. G.A.G., P.C., and R.D. aided in sample preparation and manuscript editing.

## References

Anzures B. A., Parman S. W., Milliken R. E., Lanzirotti A. and Newville M. (2020) XANES spectroscopy of sulfides stable under reducing conditions. *American Mineralogist* **105**, 375–381.

Backnaes L., Stelling J., Behrens H., Goettlicher J., Mangold S., Verheijen O., Beerkens R. G. C. and Deubener J. (2008) Dissolution Mechanisms of Tetravalent Sulphur in Silicate Melts: Evidences from Sulphur K Edge XANES Studies on Glasses. *Journal of the American Ceramic Society* **91**, 721–727.

Bajt S., Sutton S. R. and Delaney J. S. (1994) X-ray microprobe analysis of iron oxidation states in silicates and oxides using X-ray absorption near edge structure (XANES). *Geochimica et Cosmochimica Acta* **58**, 5209–5214.

Baker D. R. and Moretti R. (2011) Modeling the solubility of sulfur in magmas: a 50-year old geochemical challenge. *Reviews in Mineralogy and Geochemistry* **73**, 167–213.

Barnes J. D., Prather T. J., Cisneros M., Befus K., Gardner J. E. and Larson T. E. (2014) Stable chlorine isotope behavior during volcanic degassing of $H_2O$ and $CO_2$ at Mono Craters, CA. *Bulletin of Volcanology* **76**, 805.

Berry A. J., Danyushevsky L. V., O'Neill H. S. C., Newville M. and Sutton S. R. (2008) Oxidation state of iron in komatiitic melt inclusions indicates hot Archaean mantle. *Nature* **455**, 960.

Berry A. J., O'Neill H. St. C., Jayasuriya K. D., Campbell S. J. and Foran G. J. (2003) XANES calibrations for the oxidation state of iron in a silicate glass. *American Mineralogist* **88**, 967–977.

Berry A. J., Stewart G. A., O'Neill H. S. C., Mallmann G. and Mosselmans J. F. W. (2018) A re-assessment of the oxidation state of iron in MORB glasses. *Earth and Planetary Science Letters* **483**, 114–123.

Blundy, J., Melekhova, E., Ziberna, L., Humphreys, M.C.S., Cerantola, V., Brooker, R.A., McCammon, C.A., Pichavant, M., Ulmer, P., 2020. Effect of redox on Fe–Mg–Mn exchange between olivine and melt and an oxybarometer for basalts. Contrib. to Mineral. Petrol. **175,** 11.

Bonnin-Mosbah M., Métrich N., Susini J., Salomé M., Massare D. and Menez B. (2002) Micro X-ray absorption near edge structure at the sulfur and iron K-edges in natural silicate glasses. *Spectrochimica Acta Part B: Atomic Spectroscopy* **57**, 711–725.

Bonnin-Mosbah M., Simionovici A. S., Métrich N., Duraud J.-P., Massare D. and Dillmann P. (2001) Iron oxidation states in silicate glass fragments and glass inclusions with a XANES micro-probe. *Journal of Non-Crystalline Solids* **288**, 103–113.

1144 Borisov A., Behrens H. and Holtz F. (2018) Ferric/ferrous ratio in silicate melts: A new model
1145 for 1 atm data with special emphasis on the effects of melt composition. *Contributions to*
1146 *Mineralogy and Petrology* **173**, 98.

1147 Botcharnikov R. E., Linnen R. L., Wilke M., Holtz F., Jugo P. J. and Berndt J. (2011) High gold
1148 concentrations in sulphide-bearing magma under oxidizing conditions. *Nature Geosci* **4**,
1149 112–115.

1150 Brounce M. N., Boyce J., McCubbin F. M., Humphreys J., Reppart J., Stolper E. and Eiler J.
1151 (2019) The oxidation state of sulfur in lunar apatite. *American Mineralogist* **104**, 307–
1152 312.

1153 Brounce M. N., Kelley K. A. and Cottrell E. (2014) Variations in $Fe^{3+}/\Sigma Fe$ of Mariana Arc
1154 basalts and mantle wedge $fO_2$. *Journal of Petrology* **55**, 2513–2536.

1155 Brounce M. N., Stolper E. and Eiler J. (2017) Redox variations in Mauna Kea lavas, the oxygen
1156 fugacity of the Hawaiian plume, and the role of volcanic gases in Earth's oxygenation.
1157 *Proceedings of the National Academy of Sciences* **114**, 8997–9002.

1158 Browaeys J. (2021) *Linear fit with both uncertainties in x and in y.*, MATLAB Central File
1159 Exchange.

1160 Callegaro S., Geraki K., Marzoli A., Min A. D., Maneta V. and Baker D. R. (2020) The quintet
1161 completed: The partitioning of sulfur between nominally volatile-free minerals and
1162 silicate melts. *American Mineralogist* **105**, 697–707.

1163 Carroll M. and Rutherford M. J. (1988) Sulfur speciation in hydrous experimental glasses of
1164 varying oxidation state–results from measured wavelength shifts of sulfur X-rays.
1165 *American Mineralogist* **73**, 845–9.

1166 Castro J. M., Dingwell D. B., Nichols A. R. and Gardner J. E. (2005) New insights on the origin
1167 of flow bands in obsidian. In *Kinematics and dynamics of lava flows* (eds. M. Manga and
1168 G. Ventura). Special Papers-Geological Society of America. Boulder, Colo.; Geological
1169 Society of America; 1999. pp. 55–65.

1170 Chowdhury P. and Dasgupta R. (2019) Effect of sulfate on the basaltic liquidus and Sulfur
1171 Concentration at Anhydrite Saturation (SCAS) of hydrous basalts–Implications for sulfur
1172 cycle in subduction zones. *Chemical Geology* **522**, 162–174.

1173 Cottrell E., Birner S., Brounce M. N., Davis F. A., Waters L. E. and Kelley K. A. (2020) Oxygen
1174 Fugacity Across Tectonic Settings. In *Redox variables and mechanisms in magmatism*
1175 *and volcanism* (eds. D. R. Neuville and R. Moretti). AGU Geophysical Monograph.
1176 Wiley.

1177 Cottrell E. and Kelley K. A. (2011) The oxidation state of Fe in MORB glasses and the oxygen
1178 fugacity of the upper mantle. *Earth and Planetary Science Letters* **305**, 270–282.

Cottrell E., Kelley K. A., Lanzirotti A. and Fischer R. A. (2009) High-precision determination of iron oxidation state in silicate glasses using XANES. *Chemical Geology* **268**, 167–179.

Cottrell E., Lanzirotti A., Mysen B., Birner S., Kelley K. A., Botcharnikov R., Davis F. A. and Newville M. (2018) A Mössbauer-based XANES calibration for hydrous basalt glasses reveals radiation-induced oxidation of Fe. *American Mineralogist* **103**, 489–501.

Danyushevsky L. V., McNeill A. W. and Sobolev A. V. (2002) Experimental and petrological studies of melt inclusions in phenocrysts from mantle-derived magmas: An overview of techniques, advantages and complications. *Chemical Geology* **183**, 5–24.

Dauphas N., Roskosz M., Alp E. E., Neuville D. R., Hu M. Y., Sio C. K., Tissot F. L. H., Zhao J., Tissandier L. and Médard E. (2014) Magma redox and structural controls on iron isotope variations in Earth's mantle and crust. *Earth and Planetary Science Letters* **398**, 127–140.

Deubener J., Müller R., Behrens H. and Heide G. (2003) Water and the glass transition temperature of silicate melts. *Journal of Non-Crystalline Solids* **330**, 268–273.

Di Genova, D., Brooker, R.A., Mader, H.M., Drewitt, J.W.E., Longo, A., Deubener, J., Neuville, D.R., Fanara, S., Shebanova, O., Anzellini, S., Arzilli, F., Bamber, E.C., Hennet, L., La Spina, G., Miyajima, N., 2020. In situ observation of nanolite growth in volcanic melt: a driving force for explosive eruptions. Sci. Adv. **6**, 39, eabb0413.

Di Genova D., Caracciolo A. and Kolzenburg S. (2018) Measuring the degree of "nanotilization" of volcanic glasses: Understanding syn-eruptive processes recorded in melt inclusions. *Lithos* **318**, 209–218.

Di Genova D., Sicola S., Romano C., Vona A., Fanara S. and Spina L. (2017) Effect of iron and nanolites on Raman spectra of volcanic glasses: A reassessment of existing strategies to estimate the water content. *Chemical Geology* **475**, 76–86.

Dyar M. D., McCanta M., Breves E., Carey C. J. and Lanzirotti A. (2016) Accurate predictions of iron redox state in silicate glasses: A multivariate approach using X-ray absorption spectroscopy. *American Mineralogist* **101**, 744–747.

Elam W. T., Ravel B. D. and Sieber J. R. (2002) A new atomic database for X-ray spectroscopic calculations. *Radiation Physics and Chemistry* **63**, 121–128.

Farges F., Lefrère Y., Rossano S., Berthereau A., Calas G. and Brown G. E. (2004) The effect of redox state on the local structural environment of iron in silicate glasses: a combined XAFS spectroscopy, molecular dynamics, and bond valence study. *Journal of Non-Crystalline Solids* **344**, 176–188.

Farges F., Munoz M., Siewert R., Malavergne V., Brown G. E., Behrens H., Nowak M. and Petit P.-E. (2001) Transition elements in water-bearing silicate glasses/melts. part II. Ni in water-bearing glasses. *Geochimica et Cosmochimica Acta* **65**, 1679–1693.

Fiege A., Holtz F., Shimizu N., Mandeville C. W., Behrens H. and Knipping J. L. (2014) Sulfur isotope fractionation between fluid and andesitic melt: An experimental study. *Geochimica et Cosmochimica Acta* **142**, 501–521.

Fiege A., Ruprecht P., Simon A. C., Bell A. S., Göttlicher J., Newville M., Lanzirotti T. and Moore G. (2017) Calibration of Fe XANES for high-precision determination of Fe oxidation state in glasses: Comparison of new and existing results obtained at different synchrotron radiation sources. *American Mineralogist* **102**, 369–380.

Fleet M. E., Liu X., Harmer S. L. and King P. L. (2005) Sulfur K-edge XANES spectroscopy: Chemical state and content of sulfur in silicate glasses. *The Canadian Mineralogist* **43**, 1605–1618.

Gaborieau M., Laubier M., Bolfan-Casanova N., McCammon C. A., Vantelon D., Chumakov A. I., Schiavi F., Neuville D. R. and Venugopal S. (2020) Determination of $Fe^{3+}/\Sigma Fe$ of olivine-hosted melt inclusions using Mössbauer and XANES spectroscopy. *Chemical Geology* **547**, 119646.

Gaetani G. A., O'Leary J. A., Shimizu N., Bucholz C. E. and Newville M. (2012) Rapid reequilibration of $H_2O$ and oxygen fugacity in olivine-hosted melt inclusions. *Geology* **40**, 915–918.

Galoisy L. and Calas G. (2021) The unique speciation of iron in calc-alkaline obsidians. *Chemical Geology* **559**, 119925.

Galoisy L., Calas G. and Arrio M. A. (2001) High-resolution XANES spectra of iron in minerals and glasses: structural information from the pre-edge region. *Chemical geology* **174**, 307–319.

Gonçalves Ferreira P., de Ligny D., Lazzari O., Jean A., Gonzalez O. C. and Neuville D. R. (2013) Photoreduction of iron by a synchrotron X-ray beam in low iron content soda-lime silicate glasses. *Chemical Geology* **346**, 106–112.

Graz Y., Scaillet B., Pichavant M. and Gaillard F. (2007) The effect of sulfur on the $Fe^{2+}/Fe^{3+}$ ratio of MORB and its implications for the redox state of the mantle.

Grocke S. B., Cottrell E., de Silva S. and Kelley K. A. (2016) The role of crustal and eruptive processes versus source variations in controlling the oxidation state of iron in Central Andean magmas. *Earth and Planetary Science Letters* **440**, 92–104.

Head E., Lanzirotti A., Newville M. and Sutton S. (2018) Vanadium, sulfur, and iron valences in melt inclusions as a window into magmatic processes: A case study at Nyamuragira volcano, Africa. *Geochimica et Cosmochimica Acta* **226**, 149–173.

Helz R. T., Cottrell E., Brounce M. N. and Kelley K. A. (2017) Olivine-melt relationships and syneruptive redox variations in the 1959 eruption of Kīlauea Volcano as revealed by XANES. *Journal of Volcanology and Geothermal Research* **333**, 1–14.

Hughes E. C., Buse B., Kearns S. L., Blundy J. D., Kilgour G., Mader H. M., Brooker R. A., Balzer R., Botcharnikov R. E. and Di Genova D. (2018) High spatial resolution analysis of the iron oxidation state in silicate glasses using the electron probe. *American Mineralogist: Journal of Earth and Planetary Materials* **103**, 1473–1486.

Hughes E. C., Buse B., Kearns S. L., Brooker R. A., Di Genova D., Kilgour G., Mader H. M. and Blundy J. D. (2020) The microanalysis of iron and sulphur oxidation states in silicate glass-Understanding the effects of beam damage. In *IOP Conference Series: Materials Science and Engineering* IOP Publishing. p. 012014.

Jarosewich E., Nelen J. A. and Norberg J. A. (1980) Reference samples for electron microprobe analysis. *Geostandards Newsletter* **4**, 43–47.

Jégo S. and Dasgupta R. (2014) The fate of sulfur during fluid-present melting of subducting basaltic crust at variable oxygen fugacity. *Journal of Petrology* **55**, 1019–1050.

Jugo P. J. (2009) Sulfur content at sulfide saturation in oxidized magmas. *Geology* **37**, 415–418.

Jugo P. J., Wilke M. and Botcharnikov R. E. (2010) Sulfur K-edge XANES analysis of natural and synthetic basaltic glasses: Implications for S speciation and S content as function of oxygen fugacity. *Geochimica et Cosmochimica Acta* **74**, 5926–5938.

Kelley K. A. and Cottrell E. (2012) The influence of magmatic differentiation on the oxidation state of Fe in a basaltic arc magma. *Earth and Planetary Science Letters* **329–330**, 109–121.

Kelley K. A. and Cottrell E. (2009) Water and the oxidation state of subduction zone magmas. *Science* **325**, 605–607.

Kent A. J. (2008) Melt inclusions in basaltic and related volcanic rocks. *Reviews in Mineralogy and Geochemistry* **69**, 273–331.

Klimm K., Kohn S. C. and Botcharnikov R. E. (2012a) The dissolution mechanism of sulphur in hydrous silicate melts. II: Solubility and speciation of sulphur in hydrous silicate melts as a function of $fO_2$. *Chemical Geology* **322**, 250–267.

Klimm K., Kohn S. C., O'Dell L. A., Botcharnikov R. E. and Smith M. E. (2012b) The dissolution mechanism of sulphur in hydrous silicate melts. I: Assessment of analytical techniques in determining the sulphur speciation in iron-free to iron-poor glasses. *Chemical Geology* **322**, 237–249.

Konecke B. A., Fiege A., Simon A. C., Parat F. and Stechern A. (2017) Co-variability of $S^{6+}$, $S^{4+}$, and $S^{2-}$ in apatite as a function of oxidation state: Implications for a new oxybarometer. *American Mineralogist* **102**, 548–557.

Kraft S., Stümpel J., Becker P. and Kuetgens U. (1996) High resolution x-ray absorption spectroscopy with absolute energy calibration for the determination of absorption edge energies. *Review of Scientific Instruments* **67**, 681–687.

1287 Kress V. C. and Carmichael I. S. (1991) The compressibility of silicate liquids containing $Fe_2O_3$
1288 and the effect of composition, temperature, oxygen fugacity and pressure on their redox
1289 states. *Contributions to Mineralogy and Petrology* **108**, 82–92.

1290 Kuehn S. C., Froese D. G., Shane P. A. R. and INTAV Intercomparison Participants (2011) The
1291 INTAV intercomparison of electron-beam microanalysis of glass by tephrochronology
1292 laboratories: results and recommendations. *Quaternary International* **246**, 19–47.

1293 Lanzirotti A., Lee L., Head E., Sutton S. R., Newville M., McCanta M., Lerner A. H. and
1294 Wallace P. J. (2019) Direct measurements of copper speciation in basaltic glasses:
1295 understanding the relative roles of sulfur and oxygen in copper complexation in melts.
1296 *Geochimica et Cosmochimica Acta* **267**, 164–178.

1297 Lerner A. H. (2020) The depths and locations of magma reservoirs and their consequences for
1298 the behavior of sulfur and volcanic degassing. Ph.D. Thesis, University of Oregon.

1299 Lerner A. H., Wallace P. J., Shea T., Mourey A. J., Kelly P. J., Nadeau P. A., Elias T., Kern C.,
1300 Clor L. E., Gansecki C., Lee R. L., Moore L. R. and Werner C. A. (2021) The petrologic
1301 and degassing behavior of sulfur and other magmatic volatiles from the 2018 eruption of
1302 Kīlauea, Hawai‘i: melt concentrations, magma storage depths, and magma recycling. *Bull*
1303 *Volcanol* **83**, 43.

1304 Li D., Bancroft G. M., Kasrai M., Fleet M. E., Feng X. and Tan K. (1995) S K- and L-edge X-
1305 ray absorption spectroscopy of metal sulfides and sulfates; applications in mineralogy
1306 and geochemistry. *The Canadian Mineralogist* **33**, 949–960.

1307 Ma C., Rossman G. R. and Miller J. A. (2007) The Origin of Color in “Fire” Obsidian. *The*
1308 *Canadian Mineralogist* **45**, 551–557.

1309 Manceau A. and Nagy K. L. (2012) Quantitative analysis of sulfur functional groups in natural
1310 organic matter by XANES spectroscopy. *Geochimica et Cosmochimica Acta* **99**, 206–
1311 223.

1312 Masotta M. and Keppler H. (2015) Anhydrite solubility in differentiated arc magmas.
1313 *Geochimica et Cosmochimica Acta* **158**, 79–102.

1314 Matjuschkin V., Blundy J. D. and Brooker R. A. (2016) The effect of pressure on sulphur
1315 speciation in mid-to deep-crustal arc magmas and implications for the formation of
1316 porphyry copper deposits. *Contributions to Mineralogy and Petrology* **171**, 66.

1317 McCanta M. C., Dyar M. D., Lanzirotti A., Newville M. and Breitenfeld L. B. (2019) In-situ
1318 mapping of ferric iron variations in lunar glasses using X-ray absorption spectroscopy.
1319 *American Mineralogist* **104**, 453–458.

1320 McCanta M. C., Dyar M. D., Rutherford M. J., Lanzirotti A., Sutton S. R. and Thomson B. J.
1321 (2017) In situ measurement of ferric iron in lunar glass beads using Fe-XAS. *Icarus* **285**,
1322 95–102.

Métrich N., Berry A. J., O'Neill H. S. C. and Susini J. (2009) The oxidation state of sulfur in synthetic and natural glasses determined by X-ray absorption spectroscopy. *Geochimica et Cosmochimica Acta* **73**, 2382–2399.

Métrich N., Bonnin-Mosbah M., Susini J., Menez B. and Galoisy L. (2002) Presence of sulfite (SIV) in arc magmas: Implications for volcanic sulfur emissions. *Geophysical Research Letters* **29**, 33-1-33–4.

Métrich N. and Wallace P. J. (2008) Volatile abundances in basaltic magmas and their degassing paths tracked by melt inclusions. *Reviews in Mineralogy and Geochemistry* **69**, 363–402.

de Moor J. M., Fischer T. P., Sharp Z. D., King P. L., Wilke M., Botcharnikov R. E., Cottrell E., Zelenski M., Marty B., Klimm K., Rivard C. and Ayalew D. (2013) Sulfur degassing at Erta Ale (Ethiopia) and Masaya (Nicaragua) volcanoes: Implications for degassing processes and oxygen fugacities of basaltic systems. *Geochemistry, Geophysics, Geosystems* **14**, 4076–4108.

Moussallam Y., Edmonds M., Scaillet B., Peters N., Gennaro E., Sides I. and Oppenheimer C. (2016) The impact of degassing on the oxidation state of basaltic magmas: A case study of Kīlauea volcano. *Earth and Planetary Science Letters* **450**, 317–325.

Moussallam Y., Longpré M.-A., McCammon C., Gomez-Ulla A., Rose-Koga E. F., Scaillet B., Peters N., Gennaro E., Paris R. and Oppenheimer C. (2019) Mantle plumes are oxidised. *Earth and Planetary Science Letters* **527**, 115798.

Moussallam Y., Oppenheimer C., Scaillet B., Gaillard F., Kyle P., Peters N., Hartley M., Berlo K. and Donovan A. (2014) Tracking the changing oxidation state of Erebus magmas, from mantle to surface, driven by magma ascent and degassing. *Earth and Planetary Science Letters* **393**, 200–209.

Muth M. J. and Wallace P. J. (2021) Slab-derived sulfate generates oxidized basaltic magmas in the southern Cascade arc (California, USA). *Geology*.

Myers M. L. (2017) Storage, ascent, and release of silicic magma in caldera-forming eruptions. PhD Thesis, University of Oregon.

Myers M. L., Wallace P. J., Wilson C. J., Morter B. K. and Swallow E. J. (2016) Prolonged ascent and episodic venting of discrete magma batches at the onset of the Huckleberry Ridge supereruption, Yellowstone. *Earth and Planetary Science Letters* **451**, 285–297.

Nash W. M., Smythe D. J. and Wood B. J. (2019) Compositional and temperature effects on sulfur speciation and solubility in silicate melts. *Earth and Planetary Science Letters* **507**, 187–198.

Newville M. (2013) Larch: An analysis package for XAFS and related spectroscopies. In *Journal of Physics: Conference Series* IOP Publishing. p. 012007.

O'Neill H. S. C., Berry A. J. and Mallmann G. (2018) The oxidation state of iron in Mid-Ocean Ridge Basaltic (MORB) glasses: Implications for their petrogenesis and oxygen fugacities. *Earth and Planetary Science Letters* **504**, 152–162.

Osborn E. F. (1959) Role of oxygen pressure in the crystallization and differentiation of basaltic magma. *Am J Sci* **257**, 609–647.

Papike J. J., Simon S. B., Burger P. V., Bell A. S., Shearer C. K. and Karner J. M. (2016) Chromium, vanadium, and titanium valence systematics in Solar System pyroxene as a recorder of oxygen fugacity, planetary provenance, and processes. *American Mineralogist* **101**, 907–918.

Paris E., Giuli G., Carroll M. R. and Davoli I. (2001) The valence and speciation of sulfur in glasses by X-ray absorption spectroscopy. *The Canadian Mineralogist* **39**, 331–339.

Ravel B. and Newville M. (2005) ATHENA, ARTEMIS, HEPHAESTUS: data analysis for X-ray absorption spectroscopy using IFEFFIT. *Journal of synchrotron radiation* **12**, 537–541.

Righter K., Danielson L. R., Pando K., Morris R. V., Graff T. G., Agresti D. G., Martin A. M., Sutton S. R., Newville M. and Lanzirotti A. (2013) Redox systematics of martian magmas with implications for magnetite stability. *American Mineralogist* **98**, 616–628.

Rose T. and Brown C. (2017) Status of the Smithsonian Microbeam Standards 2017 With a Discussion of the Venerable VG-2 Basalt Glass. *Microscopy and Microanalysis* **23**, 498–499.

Rose-Koga E. F., Bouvier A.-S., Gaetani G. A., Wallace P. J., Allison C. M., Andrys J. A., de la Torre CA A., Barth A., Bodnar R. J., Ajj B. G., Butters, Castillejo A., Chilson-Parks B., Choudhary B. R., Cluzel N., Cole M., Cottrell E., Daly A., Danyushevsky L. V., Cl D., Drignon M. J., France L., Gaborieau M., Garcia M. O., Gatti E., Genske F. S., Hartley, Hughes E. C., Iveson A. A., Johnson E. R., Jones M., Kagoshima T., Katzir Y., Kawaguchi M., Kawamoto T., Kelley K. A., Koornneef J. M., Kurz, Laubier M., Layne G. D., Lerner A., Lin K.-Y., Liu P.-P., Lorenzo-Merino A., Luciani N., Magalhães N., Marschall H. R., Michael P. J., Monteleone B. D., Moore L. R., Moussallam Y., Muth M., Myers M. L., Narváez D. F., Navon O., Newcombe, Arl N., Nielsen R. L., Pamukcu A., Plank T., Rasmussen D. J., Roberge J., Schiavi F., Schwartz, Kei S., Shimizu K., Shimizu N., Thomas J. B., Thompson G. T., Tucker J. M., Ustunisik G., Waelkens C., Zhang Y. and Zhou T. (2021) Silicate melt inclusions in the new millennium: A review of recommended practices for preparation, analysis, and data presentation. *Chemical Geology*, 120145.

Rowe M. C., Kent A. J. and Nielsen R. L. (2007) Determination of sulfur speciation and oxidation state of olivine hosted melt inclusions. *Chemical Geology* **236**, 303–322.

Schreiber H. D., Merkel Jr R. C., Schreiber V. L. and Balazs G. B. (1987) Mutual interactions of redox couples via electron exchange in silicate melts: models for geochemical melt systems. *Journal of Geophysical Research: Solid Earth* **92**, 9233–9245.

1397 Sharp T. G., Stevenson R. J. and Dingwell D. B. (1996) Microlites and "nanolites" in rhyolitic
1398 glass: microstructural and chemical characterization. *Bull Volcanol* **57**, 631–640.

1399 Shorttle O., Moussallam Y., Hartley M. E., Maclennan J., Edmonds M. and Murton B. J. (2015)
1400 Fe-XANES analyses of Reykjanes Ridge basalts: Implications for oceanic crust's role in
1401 the solid Earth oxygen cycle. *Earth and Planetary Science Letters* **427**, 272–285.

1402 Sutton S. R., Lanzirotti A., Newville M., Dyar M. D. and Delaney J. (2020) Oxybarometry and
1403 valence quantification based on microscale X-ray absorption fine structure (XAFS)
1404 spectroscopy of multivalent elements. *Chemical Geology* **531**, 119305.

1405 Sutton S. R., Lanzirotti A., Newville M., Rivers M. L., Eng P. and Lefticariu L. (2017) Spatially
1406 resolved elemental analysis, spectroscopy and diffraction at the GSECARS Sector at the
1407 Advanced Photon Source. *Journal of environmental quality* **46**, 1158–1165.

1408 Tassara S., Reich M., Cannatelli C., Konecke B. A., Kausel D., Morata D., Barra F., Simon A.
1409 C., Fiege A. and Morgado E. (2020) Post-melting oxidation of highly primitive basalts
1410 from the southern Andes. *Geochimica et Cosmochimica Acta* **273**, 291–312.

1411 Tuffen H., Flude S., Berlo K., Wadsworth F. and Castro J. (2021) Obsidian. In *Encyclopedia of*
1412 *Geology (Second Edition)* (eds. D. Alderton and S. A. Elias). Academic Press, Oxford.
1413 pp. 196–208.

1414 Wallace P. J., Anderson Jr A. T. and Davis A. M. (1999) Gradients in $H_2O$, $CO_2$, and exsolved
1415 gas in a large-volume silicic magma system: Interpreting the record preserved in melt
1416 inclusions from the Bishop Tuff. *Journal of Geophysical Research: Solid Earth* **104**,
1417 20097–20122.

1418 Wallace P. J. and Carmichael I. S. E. (1994) S speciation in submarine basaltic glasses as
1419 determined by measurements of SKα X-ray wavelength shifts. *American Mineralogist*
1420 **79**, 161–167.

1421 Wallace P. J., Dufek J., Anderson A. T. and Zhang Y. (2003) Cooling rates of Plinian-fall and
1422 pyroclastic-flow deposits in the Bishop Tuff: inferences from water speciation in quartz-
1423 hosted glass inclusions. *Bulletin of Volcanology* **65**, 105–123.

1424 Wallace P. J., Plank T., Bodnar R. J., Gaetani G. A. and Shea T. (2021) Olivine-Hosted Melt
1425 Inclusions: A Microscopic Perspective on a Complex Magmatic World. *Annual Review of*
1426 *Earth and Planetary Sciences* **49**.

1427 Watkins J. M., Gardner J. E. and Befus K. S. (2017) Nonequilibrium degassing, regassing, and
1428 vapor fluxing in magmatic feeder systems. *Geology* **45**, 183–186.

1429 Waychunas G. A., Apted M. J. and Brown G. E. (1983) X-ray K-edge absorption spectra of Fe
1430 minerals and model compounds: Near-edge structure. *Phys Chem Minerals* **10**, 1–9.

1431 Weaver S. L., Wallace P. J. and Johnston A. D. (2011) A comparative study of continental vs.
1432 intraoceanic arc mantle melting: Experimentally determined phase relations of hydrous
1433 primitive melts. *Earth and Planetary Science Letters* **308**, 97–106.

1434 Wilke M., Farges F., Partzsch G. M., Schmidt C. and Behrens H. (2007) Speciation of Fe in
1435 silicate glasses and melts by in-situ XANES spectroscopy. *American Mineralogist* **92**,
1436 44–56.

1437 Wilke M., Farges F., Petit P.-E., Brown Jr G. E. and Martin F. (2001) Oxidation state and
1438 coordination of Fe in minerals: An Fe K-XANES spectroscopic study. *American*
1439 *Mineralogist* **86**, 714–730.

1440 Wilke M., Jugo P. J., Klimm K., Susini J., Botcharnikov R., Kohn S. C. and Janousch M. (2008)
1441 The origin of $S^{4+}$ detected in silicate glasses by XANES. *American Mineralogist* **93**, 235–
1442 240.

1443 Wilke M., Klimm K. and Kohn S. C. (2011) Spectroscopic studies on sulfur speciation in
1444 synthetic and natural glasses. *Reviews in Mineralogy and Geochemistry* **73**, 41–78.

1445 Wilke M., Partzsch G. M., Bernhardt R. and Lattard D. (2004) Determination of the iron
1446 oxidation state in basaltic glasses using XANES at the K-edge. *Chemical Geology* **213**,
1447 71–87.

1448 Wilke M., Schmidt C., Farges F., Malavergne V., Gautron L., Simionovici A., Hahn M. and Petit
1449 P.-E. (2006) Structural environment of iron in hydrous aluminosilicate glass and melt-
1450 evidence from X-ray absorption spectroscopy. *Chemical Geology* **229**, 144–161.

1451 Zhang H. L., Cottrell E., Solheid P. A., Kelley K. A. and Hirschmann M. M. (2018)
1452 Determination of $Fe^{3+}/\Sigma Fe$ of XANES basaltic glass standards by Mössbauer
1453 spectroscopy and its application to the oxidation state of iron in MORB. *Chemical*
1454 *Geology* **479**, 166–175.

1455 Zhang H. L., Hirschmann M. M., Cottrell E., Newville M. and Lanzirotti A. (2016) Structural
1456 environment of iron and accurate determination of $Fe^{3+}/\Sigma Fe$ ratios in andesitic glasses by
1457 XANES and Mössbauer spectroscopy. *Chemical Geology* **428**, 48–58.

1458

1459

# Appendix A. Supplemental text and figures

## Fe-XANES beam damage assessment and corrections, additional figures

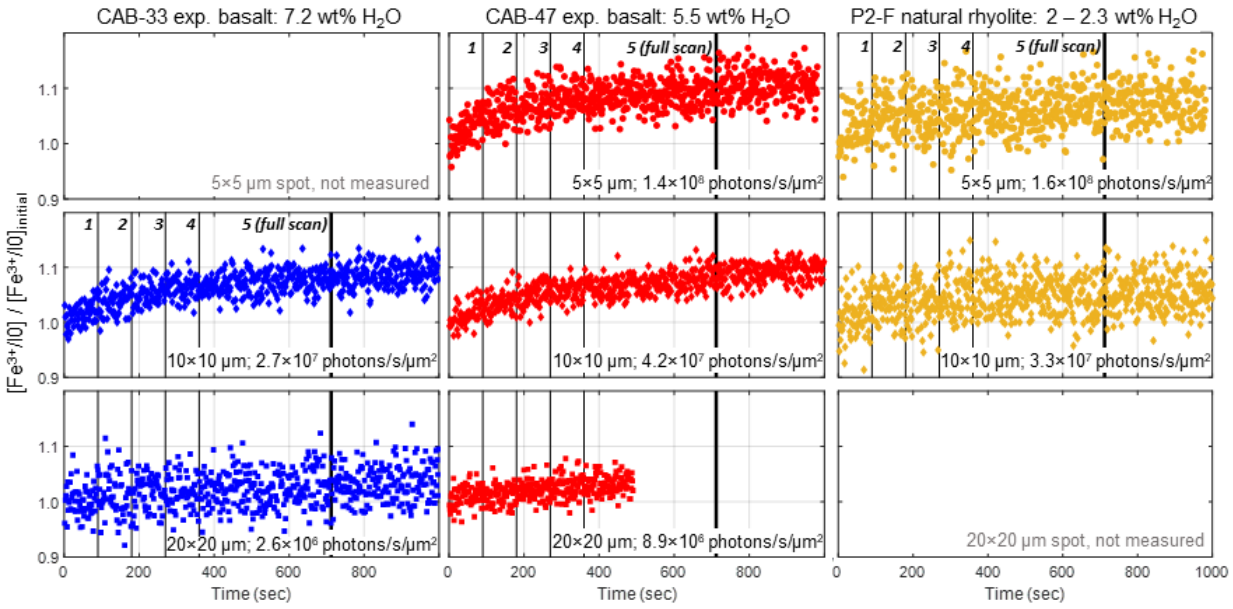


**Figure A.1**. Time dependence of the relative increase of 2nd pre-edge doublet ([Fe-*K*α/I0] / [Fe *K*α/I0$_{initial}$] at ~7113.3 eV, which we consider to be $Fe^{3+}/Fe^{3+}_{initial}$) during irradiation with X-ray beams of 5×5 µm *(upper)*, 10×10 µm *(middle)*, and 20×20 µm *(lower)* footprint sizes. $Fe^{3+}_{initial}$ is the average of the first 10 measurements (13 – 15 s of analysis). Thin vertical lines (labeled 1 – 4) indicate analysis end times for repeat pre-edge Fe-XANES analyses (0.5 s/point), as described in the text. The thick vertical line (labeled 5 full scan) is the end time after the final full energy scan. Beam damage occurs rapidly in analyses with a focused 5×5 µm beam. However, linear time-dependent functions can be regressed through the rapid scanning sequence in the first 4.5 – 6 minutes of analyses with 10×10 and 20×20 µm beams to correct beam-damaged induce oxidation to the initial (t=0 s) conditions. Photon flux densities for analyses with 5×5, 10×10, and 20×20 µm beams were 1.4 – 1.6×$10^8$, 2.7 – 4.2×$10^7$, and 2.6 – 8.9×$10^6$ photons/s/µm$^2$, respectively. We note that experimental glass CAB-33 has a spectral signature that suggests with the presence of Fe-oxide nanolites (see section **3.1**; **Data supplement**).

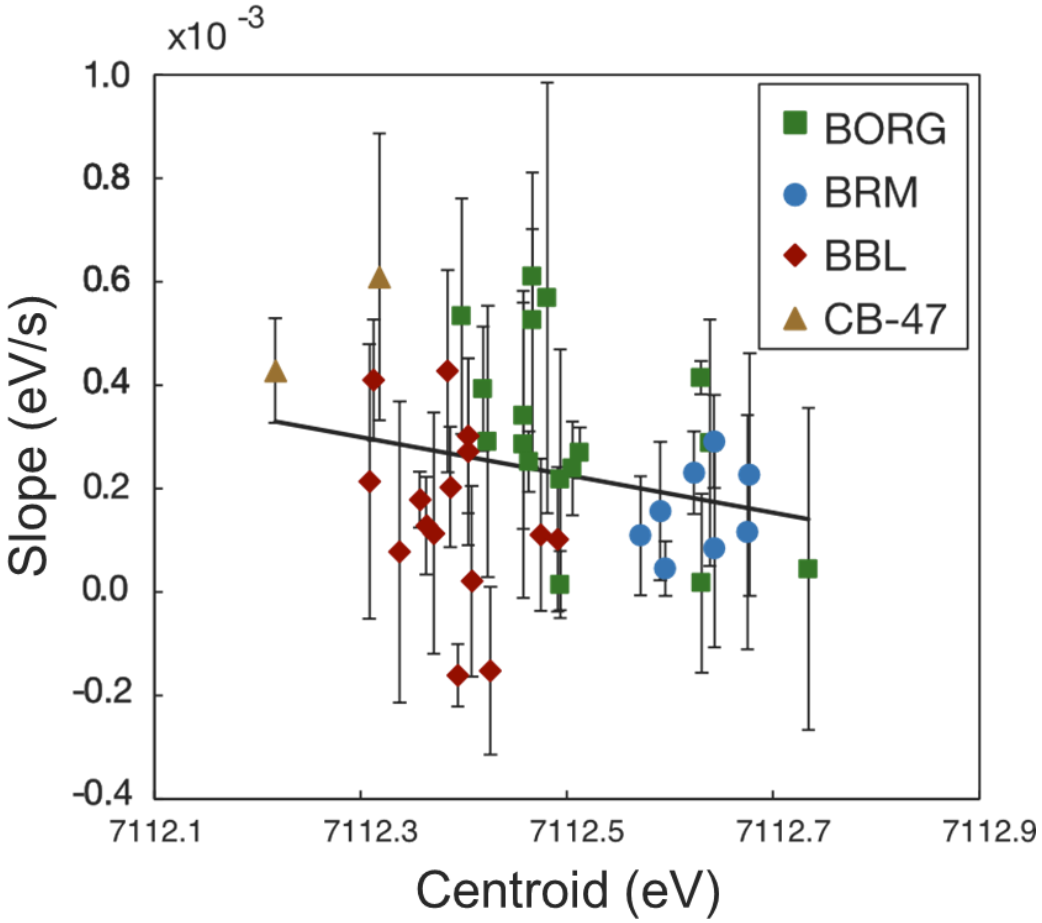


**Figure A.2**. Slopes of linear regressions through Fe-*K*α pre-edge centroid time series as a function of the centroid position of the first rapid scan (least affected by beam damage) for individual samples. The slope of each centroid linear regression can be used as a proxy for the rate of photo-oxidation. The values of these slopes show an inverse correlation with calculated initial $Fe^{3+}/\Sigma Fe$ and a positive correlation with $H_2O$ content of each glass (Figure 5), indicating that beam damage occurs more readily in reduced and/or hydrous glasses (Cottrell et al., 2018). Although the estimated initial $Fe^{3+}/\Sigma Fe$ is itself dependent on the slope of each regression, the observed correlation between slope values and $Fe^{3+}/\Sigma Fe$ is not simply an artifact; this plot shows that the centroid values of the first, least beam-damaged pre-edge scan of each analysis spot shares the same correlation between t=0 regression slopes and calculated $Fe^{3+}/\Sigma Fe$. Melt inclusions from three cinder cones in the southern Cascade arc (BORG, BRM, BBL) and experimental glasses (CAB-47) are grouped by color. Gray line represents linear fit through all data. All centroids have been shifted by +0.32 eV for consistency with the LW_0 centroid position reported by Cottrell et al. (2009). See section **2.2** for further discussion.

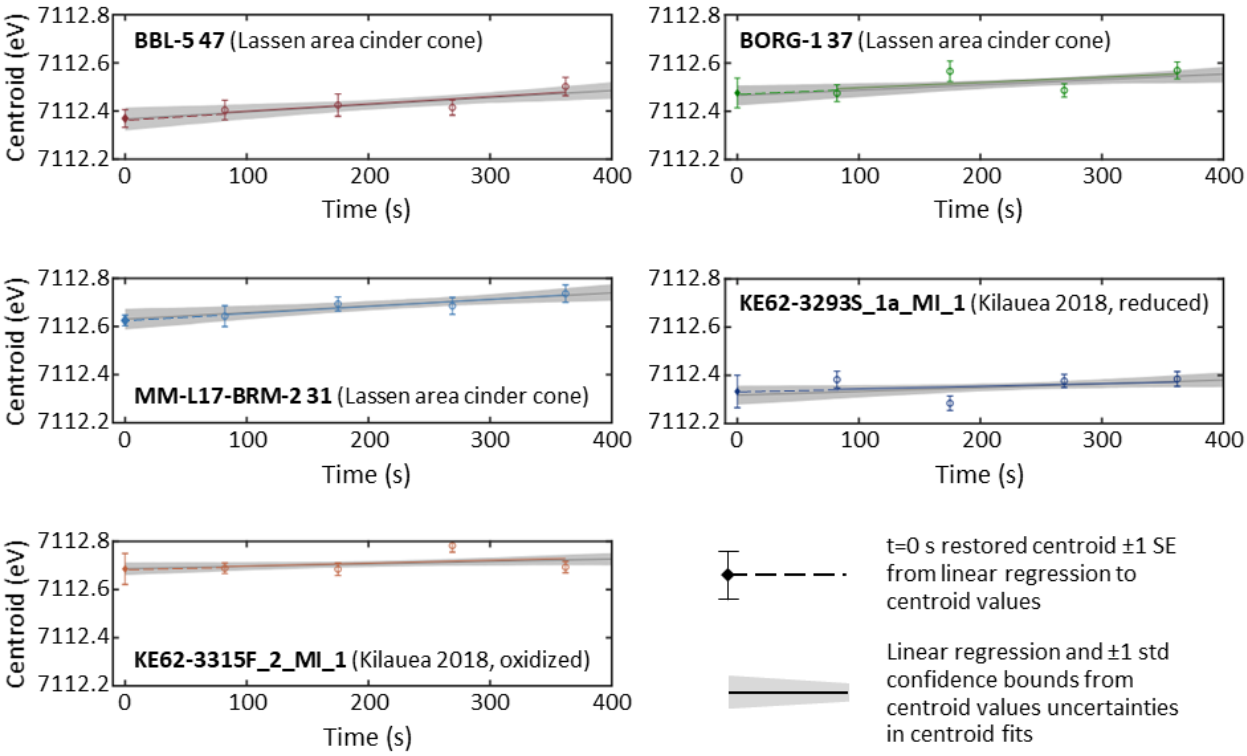


**Figure A.3**. Fe-*K*α pre-edge centroid positions calculated from repeated rapid scans of natural melt inclusions shown in Figure 4. Circles represent the centroid values calculated from one pre-edge scan. Error bars represent ±1 SE for individual centroid fits. Colored lines are linear regressions through measured centroid values from 82 to 362 s. Diamonds at t=0 s are the intercept of each linear regression to the centroid time series, and are taken to be the beam damage-corrected initial centroid position. Error bars on corrected initial centroid positions represent ±1 SE of the time series linear regression. Gray bands show ±1 standard deviation non-simultaneous prediction bounds for the linear fit function calculated using a Monte Carlo approach as described in main text. Note that the t=0 s regressions for the $H_2O$-poor Kīlauea melt inclusions are essentially flat, in contrast to the t=0 s regressions for the more hydrous (and beam damage susceptible) subduction zone melt inclusions from the Lassen area cinder cones.

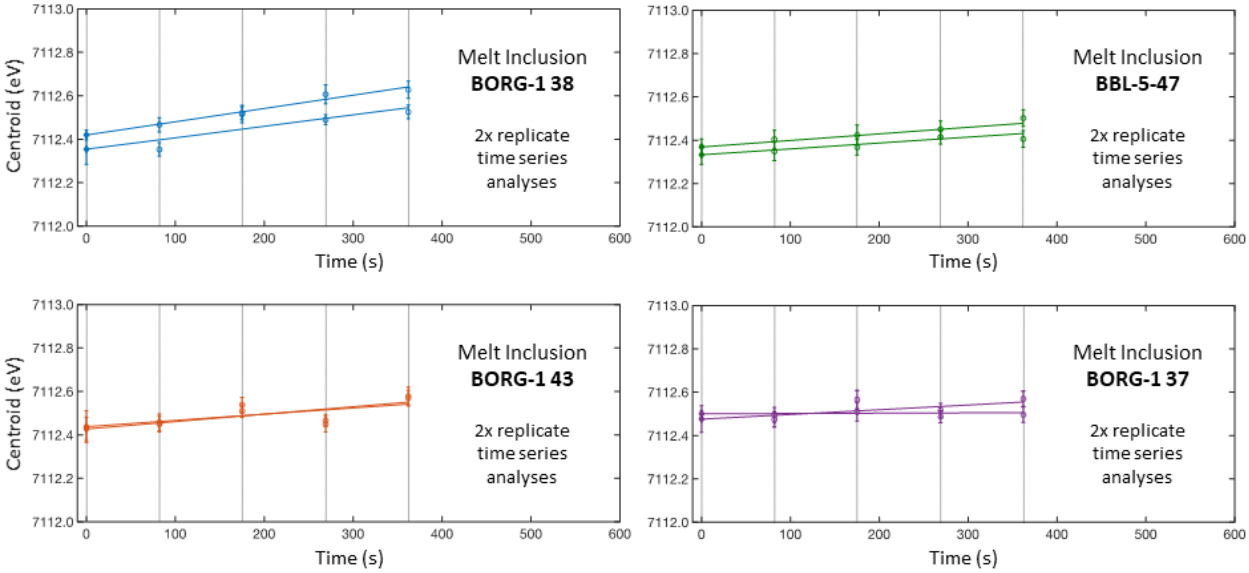


**Figure A.4**. Centroid positions calculated from replicate sets of rapid pre-edge Fe-XANES scans within single melt inclusions from the southern Cascades. Analyses were conducted with a 10×10 μm beam and photon flux densities of 3 – 5×$10^7$ photons/s/μ$m^2$. Each sequence represents repeated measurements in one analyzed spot. Open circles are centroids calculated for each pre-edge scan. Error bars represent ±1 SE of centroid fits to individual scans. Filled diamonds at t=0 s are the intercept of each linear regression and are used as the time-corrected initial centroid values. Error bars on the t=0 s centroids represent ±1 SE of each time series linear regression. Vertical lines indicate analysis end times for repeat pre-edge Fe-XANES analyses. All centroids have been shifted by +0.32 eV for consistency with the LW_0 centroid position reported by Cottrell et al. (2009).

**S-XANES peak fitting details**

Our S-XANES peak fitting approach is calibrated to the suite of experimental hydrous basaltic glasses (45 – 48 wt% $SiO_2$, 8 – 10 wt% $FeO^T$, 8 – 10 wt% CaO, 200 MPa, 1050 °C) presented in Jugo et al. (2010) (see **Data supplement**). These glasses were synthesized at different oxidation states and were used by Jugo et al. (2010) to develop an empirical fit relationship of $S^{2-}$ and $S^{6+}$ S-XANES intensities to sulfur speciation. The Jugo et al. (2010) calibration was based on the assumption that sulfur in their most reduced and oxidized end-member glasses occurred entirely as $S^{2-}$ and $S^{6+}$, respectively, and that linear combination fitting of the end-members produces representative spectra for glasses with mixed sulfur speciation. Using these end-members and linear combination mixed spectra, Jugo et al. (2010) constructed a calibration of S-XANES intensity to sulfur speciation across a range of mixed sulfur states (Figure A.5). We note that the presumed linear combination relationship between end-member sulfur-intensities and sulfur speciation has not been shown independently to be true, but in absence of confirmation from Mössbauer or wet chemistry measurements, it is currently a reasonable assumption and the results agree well with thermodynamic calculations (Jugo et al., 2010).

We use S-XANES spectra for the end-member reduced and oxidized glasses presented in Jugo et al. (2010) to construct linear mixtures of the two and create a S-XANES intensity to sulfur speciation calibration for our peak fitting method (see section **2.3** for details). The main difference between our peak fitting method and the Jugo method is that we isolate the $S^{6+}$ peak from the slightly higher energy ionization peak. By including the ionization peak in our fit procedure, we end up with no $S^{6+}$ intensity in $S^{6+}$-free glasses, whereas the Jugo et al. (2010) fit method either convolutes the $S^{6+}$ peak with the ionization peak or fits the step-function background differently than we do, which results in ~0.3 $I[S^{6+}]/I\Sigma S$ XANES intensity present in $S^{6+}$-free glasses. Applying our peak fitting to the full set of hydrous experimental glasses (200 MPa, 1050 °C, FMQ -1.4 to +2.7) presented in Jugo et al. (2010), we find good agreement between sulfur speciation calculated from our method with that of Jugo et al. (2010) (Figure A.8; see **Data supplement**).

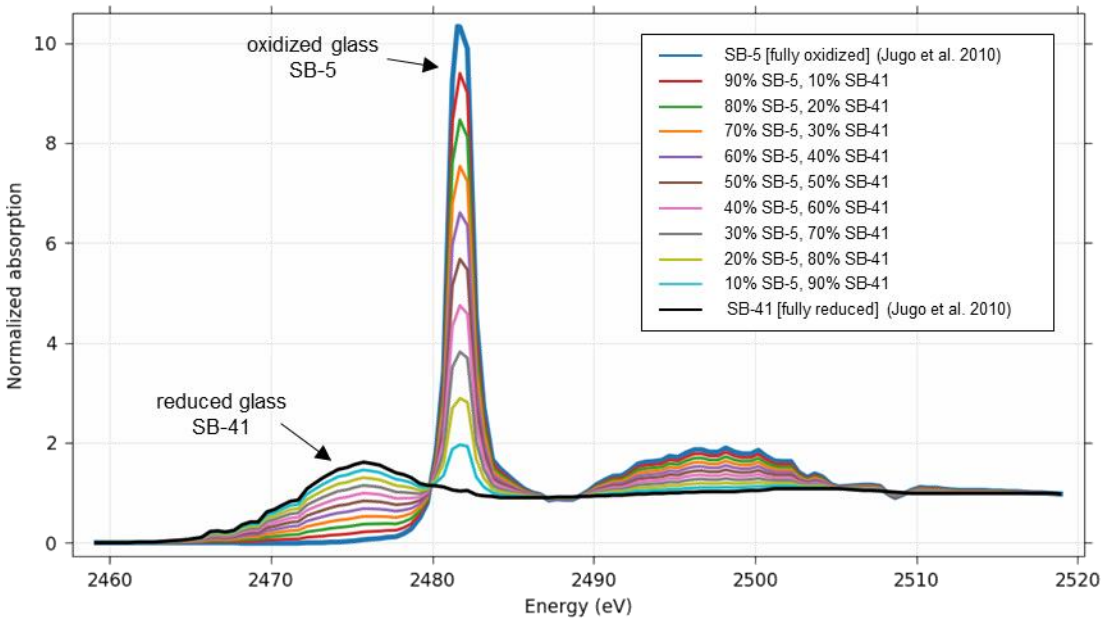


**Figure A.5**. Normalized spectra of completely oxidized (SB-5; FMQ +2.7; $S^{6+}/S\Sigma = 1.00$; blue curve) and completely reduced (SB-41; FMQ -1.4; $S^{6+}/S\Sigma = 0.00$, black curve) hydrous experimental glasses reproduced from Jugo et al. (2010) (see **Data supplement**). Linear two-component mixing of these endmember glasses provides a simulated set of spectra to calibrate S-XANES intensities to sulfur speciation in glasses in both Jugo et al. (2010) and in the peak-fitting method presented here. An energy shift of -1 eV has been applied to all the Jugo et al. (2010) data (see section **2.3.1**).

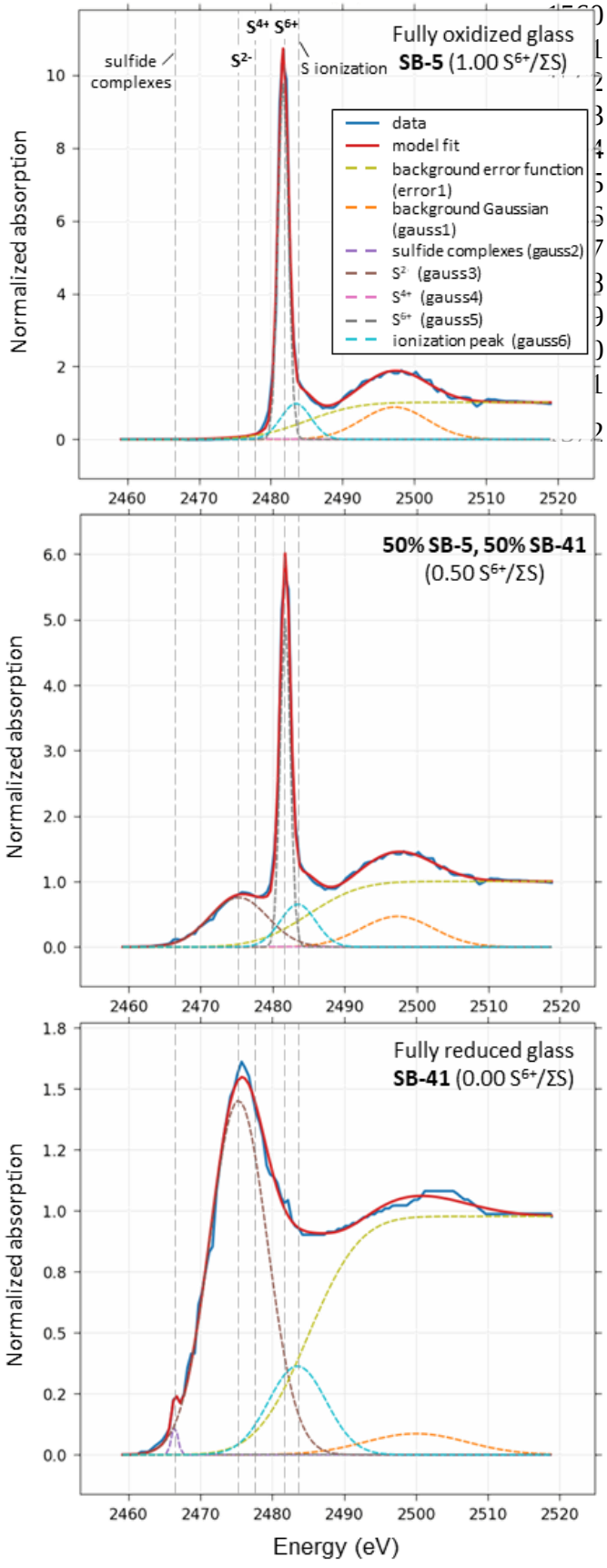


**Figure A.6**. Example peak fits to the normalized end-member oxidized *(upper)* and reduced *(lower)* hydrous experimental glasses reproduced from Jugo et al. (2010), as well as a 50% linear mixture of the two endmembers *(middle)*. Parameters of the fit functions are identified in Table 2. Reference peak position lines may vary slightly between samples. An energy shift of -1 eV has been applied to all the Jugo et al. (2010) data (see section **2.3.1**).

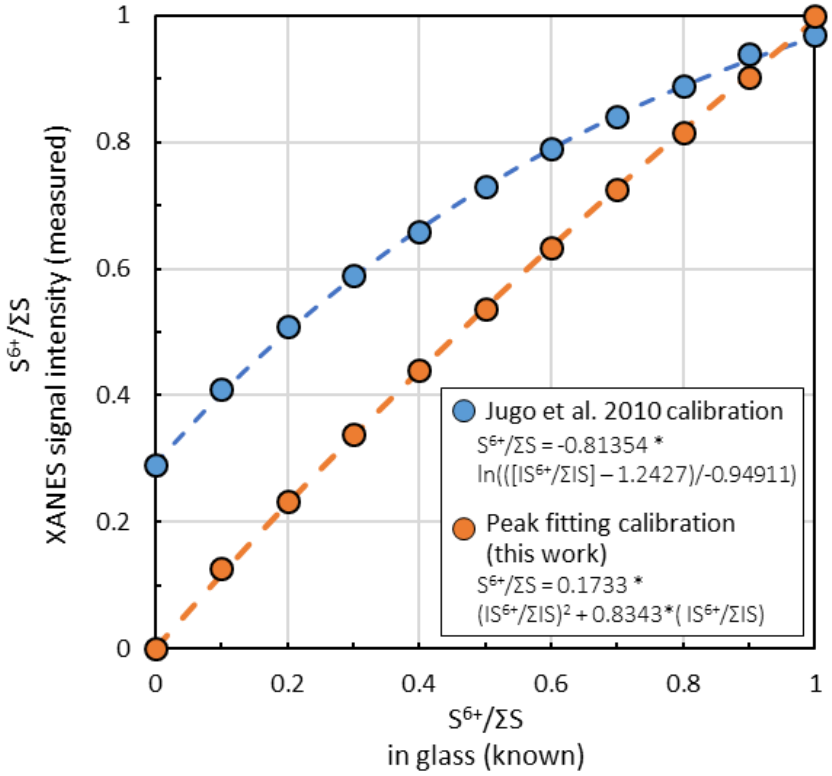


**Figure A.7**. Fit relationships between S-XANES $S^{6+}/\Sigma S$ signal intensity and $S^{6+}/\Sigma S$ speciation in experimental end-member hydrous glasses and linear component mixtures for the Jugo et al. (2010) calibration (blue) and the peak fitting calibration in this study (orange). Relative uncertainties in $S^{6+}/\Sigma S$ signal intensities from S-XANES peak fitting are estimated to be ±7% (2RSE) based on the reproducibility of spectral fitting (see **Data supplement**).

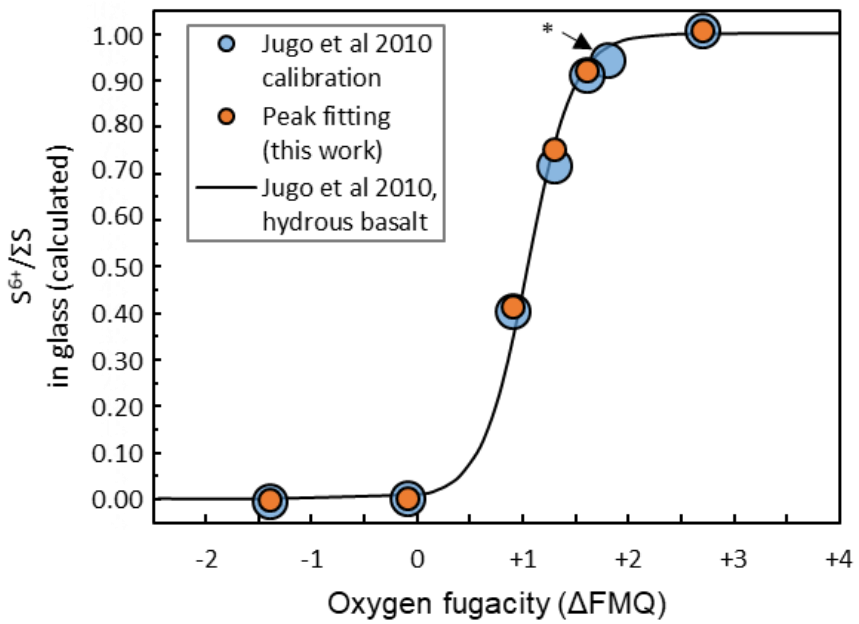


**Figure A.8**. Calculated sulfur speciation vs $fO_2$ experimental conditions of the set of synthesized hydrous glasses from Jugo et al. (2010), with XANES spectral fits from our peak fitting method (orange) compared to the Jugo et al. (2010) approach (blue) (see **Data supplement**). Only the most oxidized and reduced glasses were used to calibrate the peak fitting method. Applying our peak fitting method to the Jugo et al. (2010) suite of glass samples synthesized at intermediate $fO_2$ shows that the two methods calculate very similar $S^{6+}/\Sigma S$ values. Relative uncertainty in $S^{6+}/\Sigma S$ calculations via the peak fitting method is estimated to be ±10% based on the reproducibility of spectra normalization and fitting. The "*" symbol indicates that the normalized XANES spectrum for this glass was not presented in Jugo et al. (2010), precluding inclusion in our comparison. The black curve is the Jugo et al. (2010) predicted relation of $fO_2$ and $S^{6+}/\Sigma S$ for a hydrous basalt at 1050°C and 200 MPa.

## Appendix References

Cottrell E., Kelley K. A., Lanzirotti A. and Fischer R. A. (2009) High-precision determination of iron oxidation state in silicate glasses using XANES. *Chemical Geology* **268**, 167–179.

Cottrell E., Lanzirotti A., Mysen B., Birner S., Kelley K. A., Botcharnikov R., Davis F. A. and Newville M. (2018) A Mössbauer-based XANES calibration for hydrous basalt glasses reveals radiation-induced oxidation of Fe. *American Mineralogist* **103**, 489–501.

Jugo P. J., Wilke M. and Botcharnikov R. E. (2010) Sulfur K-edge XANES analysis of natural and synthetic basaltic glasses: Implications for S speciation and S content as function of oxygen fugacity. *Geochimica et Cosmochimica Acta* **74**, 5926–5938.